Check for updates

INFECTIOUS DISEASES

Copyright © 2026 The Authors, some rights reserved; exclusive licensee American Association for the Advancement of Science. No claim to original U.S. Government Works

Orthogonal Fc engineering enables multiplexed delivery of mRNA-encoded bispecific antibodies that constrain viral escape

Anna Z. Wec[1]†, Alice Cho[1]†, Simone Pecetta[1]†, Xiaozhen Hu[1], Michael F. Bender[1], Adrian R. Laciak[1], Jacob Hou[1], Fanchong Jian[2], Elif N. Korkmaz[1], Arvind Sharma[1], Nathen Bopp[1], Steve Sazinsky[1], Daniela Montes-Berrueta[1], Tessa Speidel[1], Diana Lee[1], Pradeep Babu Jagadeesh Reddy[1], Yunlong Cao[2,3,4], Andrea Carfi[1], William R. Schief[1,5,6,7], Laura M. Walker[1]*

The continuous antigenic evolution of severe acute respiratory syndrome coronavirus 2 (SARS-CoV-2) has repeatedly undermined the effectiveness of monoclonal antibody (mAb) therapies, underscoring the need for innovative approaches that improve therapeutic mAb breadth and durability of protection. Here, we engineered messenger ribonucleic acid (mRNA)–encoded bispecific antibodies (bsAbs) that, upon intravenous administration in lipid nanoparticles, achieved high serum concentrations, extended half-life, and serum neutralizing titers exceeding 1:10,000 in human neonatal Fc receptor (FcRn)–expressing mice. To enhance resilience to viral escape, we used structure-guided computational design to introduce Fc modifications that promoted selective homodimerization, thereby enabling codelivery of multiple mRNA-encoded bsAbs with cognate heavy chain pairing. In vivo expression of a triple bsAb combination resulted in broad serum neutralization of historical and contemporary SARS-CoV-2 variants, including the highly mutated BA.3.2.2 lineage. Preexposure prophylaxis with the mRNA-delivered bsAb combination conferred protection against SARS-CoV-2 XBB.1.5 challenge, preventing weight loss and decreasing viral burden in the lungs compared with vehicle control treatment. Together, the results provide proof of principle for mRNA-based delivery of Fc-engineered bsAb combinations to combat SARS-CoV-2 and potentially other rapidly evolving pathogens.

INTRODUCTION

Coronavirus disease 2019 (COVID-19) remains an important public health concern, particularly for immunocompromised individuals who mount suboptimal immune responses to vaccination and face an elevated risk of severe disease (*1*). Several monoclonal antibodies (mAbs) targeting the severe acute respiratory syndrome coronavirus 2 (SARS-CoV-2) receptor binding domain (RBD) initially demonstrated a high degree of efficacy in both treatment and prophylaxis of COVID-19 in high-risk populations (*2*–*5*); however, all first-generation monotherapies and two-mAb cocktails rapidly lost effectiveness because of the emergence of SARS-CoV-2 escape variants (*6*, *7*). Furthermore, despite the recent establishment of an expedited regulatory pathway for emergency use authorization of anti-SARS-CoV-2 mAbs (*8*), the dynamic SARS-CoV-2 variant landscape continues to undermine the development of next-generation mAbs. For example, the second-generation anti-RBD monotherapies pemivibart (also known as Pemgarda or VYD222) and sipavibart demonstrated prophylactic efficacy against sensitive variants in phase 3 clinical studies (*8*, *9*), but both mAbs have since lost substantial activity against certain JN.1-derived subvariants (*10*, *11*), underscoring the distinct challenges associated with the development of traditional mAb therapies against rapidly evolving viruses such as SARS-CoV-2.

Bispecific antibody (bsAb) engineering has emerged as a promising approach to enhance antiviral antibody potency and resilience to escape through increased binding valency and multiepitope targeting (*12*). However, the high cost and complexity associated with manufacturing recombinant bsAbs have hindered their development for infectious disease indications, with few candidates advancing to clinical trials and none yet receiving regulatory approval (*13*). Moreover, although bsAbs can improve breadth and potency relative to conventional immunoglobulin G (IgG) monotherapies and two-antibody cocktails, many previously described bsAbs retain vulnerabilities to emerging viral variants (*14*–*16*). Here, we addressed these manufacturing challenges and further expanded the breadth of antigenic coverage by leveraging messenger ribonucleic acid (mRNA)–lipid nanoparticle (LNP) platform technology to deliver combinations of fragment crystallizable (Fc)–engineered bsAbs in vivo. Our results establish a framework for the development of next-generation bsAb combination therapies with improved breadth and durability of protection against antigenically variable pathogens.

RESULTS

Discovery of broad and potent anti–SARS-CoV-2 HCAbs using a high-throughput functional screening platform

Prior studies have demonstrated that SARS-CoV-2 evolution is primarily driven by immune pressure from serum neutralizing antibodies targeting epitopes conserved between ancestral strains and

[1]Moderna Inc., Cambridge, MA 02142, USA. [2]Biomedical Pioneering Innovation Center (BIOPIC), Peking University, Beijing, China. [3]Changping Laboratory, Beijing, China. [4]Peking-Tsinghua Center for Life Sciences, Tsinghua University, Beijing, China. [5]IAVI Neutralizing Antibody Center, Scripps Research Institute, La Jolla, CA 92037, USA. [6]Center for HIV/AIDS Vaccine Development, Scripps Research Institute, La Jolla, CA 92037, USA. [7]Department of Immunology and Microbiology, Scripps Research Institute, La Jolla, CA 92037, USA.
†These authors contributed equally to this work.
*Corresponding author. Email: laura.walker@modernatx.com

Downloaded from https://www.science.org at Cambridge University on October 18, 2026

contemporary variants (*17*, *18*). Therefore, we sought to identify heavy chain antibodies (HCAbs) with broad reactivity across Omicron subvariants but minimal or no cross-reactivity with ancestral strains. Such antibodies are rare in human serological repertoires, suggesting that their corresponding epitopes may be under reduced immune pressure and thus less prone to circulating viral escape (*19*).

To induce an Omicron lineage–focused B cell response, we immunized three llamas with prefusion-stabilized XBB.1.5 spike mRNA and subsequently boosted them with a series of recombinant spike and RBD proteins representing more recently emerged Omicron variants and the more distantly related SARS-CoV to drive breadth of activity (Fig. 1A and fig. S1, A and B). After a final boost with SARS-CoV-2 BA.2.86 RBD, we single-cell sorted ~1700 XBB.1.5/BA.2.86 cross-reactive B cells expressing heavy chain (HC)–only antibodies containing variable heavy domains (VHHs) into 96-well plates containing feeder cells in medium supplemented with interleukin-2 (IL-2) and IL-21 to promote differentiation into antibody-secreting plasma cells (Fig. 1A and fig. S1, C and D). B cell culture supernatants were screened for binding reactivity against a large panel of SARS-CoV-2 variants and neutralizing activity against XBB.1.5 and JN.1. A large proportion of B cell supernatants showed broad reactivity, with 63.7% cross-neutralizing XBB.1.5 and JN.1 (fig. S2, A and B). We recovered VHH region sequences from the B cells expressing cross-neutralizing HCAbs, resulting in 422 unique VHH sequences representing 95 clonal lineages (fig. S2C).

A total of 127 unique clones were expressed recombinantly for further characterization (data file S1). Six clones (MOD225, MOD197, MOD242, MOD203, MOD239, and MOD185) displayed broad and potent neutralizing activity, extending from early Omicron variants through NB.1.8.1, and were subsequently humanized to reduce their potential for immunogenicity (Fig. 1B). Against post-JN.1 variants, the six HCAbs showed activity comparable or superior to that of the benchmark broadly neutralizing antibodies (bnAbs) BD55-1205 and VYD222. (Fig. 1B) (*8*, *19*). Epitope mapping studies using a combination of cross-competition, deep mutational scanning (DMS), and viral escape assays revealed that the six lead HCAbs recognized two distinct antigenic sites, both overlapping the human angiotensin-converting enzyme 2 (hACE2)–binding interface (Fig. 1C and fig. S3, A and B). Five of the six HCAbs (MOD197, MOD242, MOD203, MOD239, and MOD185) belonged to the previously described epitope group B, defined by escape mutations at positions 486 and 487 (*7*, *19*). The sixth antibody, MOD225, belonged to epitope group F3, characterized by sensitivity to mutations at positions 503, 504, and 505 (fig. S3, A and B).

We determined three high-resolution crystal structures of representative B epitope– and F3 epitope–targeting HCAbs in complex with the KP.3 RBD: MOD203 (1.90 Å), which targeted the B epitope; MOD239 (2.10 Å), also targeting the B epitope; and MOD225 (2.35 Å), which targeted the F3 epitope (Fig. 1D and table S1). KP.3 was selected for structural studies because it was the dominant variant at the time these studies were performed. We were unable to obtain crystals of sufficient quality for the most potent B epitope–targeting HCAb (MOD197); therefore, MOD203 was selected as a structural surrogate on the basis of its shared escape mutations. The footprints of MOD203 and MOD239 lie on the tip of the receptor binding motif (RBM) and overlap the ACE2 interface (Fig. 1D). Although derived from different parental clones, both HCAbs exhibited convergent modes of recognition, with RBD residues 476, 477, 486, and 487 positioned in both binding footprints. These residues were among the strongest contributors to activity in DMS and neutralization-escape experiments (fig. S3, A and B), suggesting that other B-epitope HCAbs identified through DMS (e.g., MOD197) also converge on this site. In contrast, the footprint of MOD225 overlaps that of the rare bnAb ADG-2 (and its clinical variant ADG20) (*20*) (fig. S3C). ADG20 shows reduced activity against Omicron variants carrying Asn^{501}→Tyr (N501Y) and Tyr^{505}→His (Y505H) mutations (*21*), whereas MOD225 depends on Tyr^{501} (Y501) for binding and is intolerant to Y505, providing a structural rationale for its inactivity against ancestral strains (fig. S3D). Structural superposition of RBDs bound to B- and F3-epitope VHHs revealed mild steric clashes, suggesting that simultaneous binding to the same RBD is disfavored (fig. S3E). In summary, we identified several potent Omicron cross-reactive HCAbs from immunized llamas that target two distinct antigenic sites in the ACE2 footprint of the SARS-CoV-2 RBD.

Tetravalent bsAbs display enhanced potency, breadth, and resistance to viral escape

We next sought to engineer bsAbs from the six lead HCAbs by combining the variable domains (VHHs) of antibodies targeting distinct epitopes. To achieve this, we paired VHHs targeting epitope B (MOD197, MOD242, MOD203, or MOD239) with the F3 epitope–targeting VHH (MOD225) in two different bispecific tetravalent formats ($n = 8$) (Fig. 2A). To expand epitope and bsAb format diversity, we also designed nine IgG-based bsAbs by fusing B epitope– or F3 epitope–targeting VHH domains to the HC or light chain (LC) C terminus of the previously characterized broadly neutralizing IgG BD55-1205, which belongs to epitope group A1 and exhibits exceptional neutralization breadth and barrier to in vitro escape (*19*) (Fig. 2A). In addition, we constructed eight bsAbs composed only of VHHs targeting epitope B to assess whether multivalency could compensate for the reduced activity of the parental clones against shared escape mutants. In total, we engineered 25 unique bsAbs spanning four distinct formats.

The recombinant bsAbs showed 3- to 52-fold improved potency compared with their corresponding parental antibodies, with neutralization half-maximal inhibitory concentration (IC_{50}) values ranging from 0.8 to 40.8 pM against KP.3 (Fig. 2, B and C). To assess whether the bsAbs also exhibited enhanced resilience to viral escape, we measured their neutralization IC_{50} values against viral escape mutants known to affect one or both parental clones. Although bsAbs composed of B epitope–targeting VHHs achieved higher neutralization potencies against KP.3 compared with B/F3-targeting bsAbs, their activities were abrogated by a single escape mutation [Asn^{487}→Ser (N487S) or Asn^{487}→Thr (N487T)] (Fig. 2C). In contrast, bsAbs composed of A1/F3, A1/B, and B/F3 epitope–targeting clones retained activity against escape mutants that substantially reduced activity of one or both parental antibodies. For example, although BD55-1205 and MOD197 showed relatively weak neutralizing activity against KP.3 + A475V (Ala^{475}→Val; IC_{50} values of 455 and 100 pM, respectively), the corresponding bsAbs maintained potent neutralization against this mutant, with IC_{50} values of 7 and 31 pM. Many of the bsAbs also maintained high potency against naturally occurring SARS-CoV-2 variants that showed reduced susceptibility to both parental clones, e.g., DV.7.1 (Fig. 2C). Overall, 17 of 25 bsAbs exhibited improved potency, breadth, and barrier to escape relative to the corresponding parental monotherapies.

Downloaded from https://www.science.org at Cambridge University on October 18, 2026

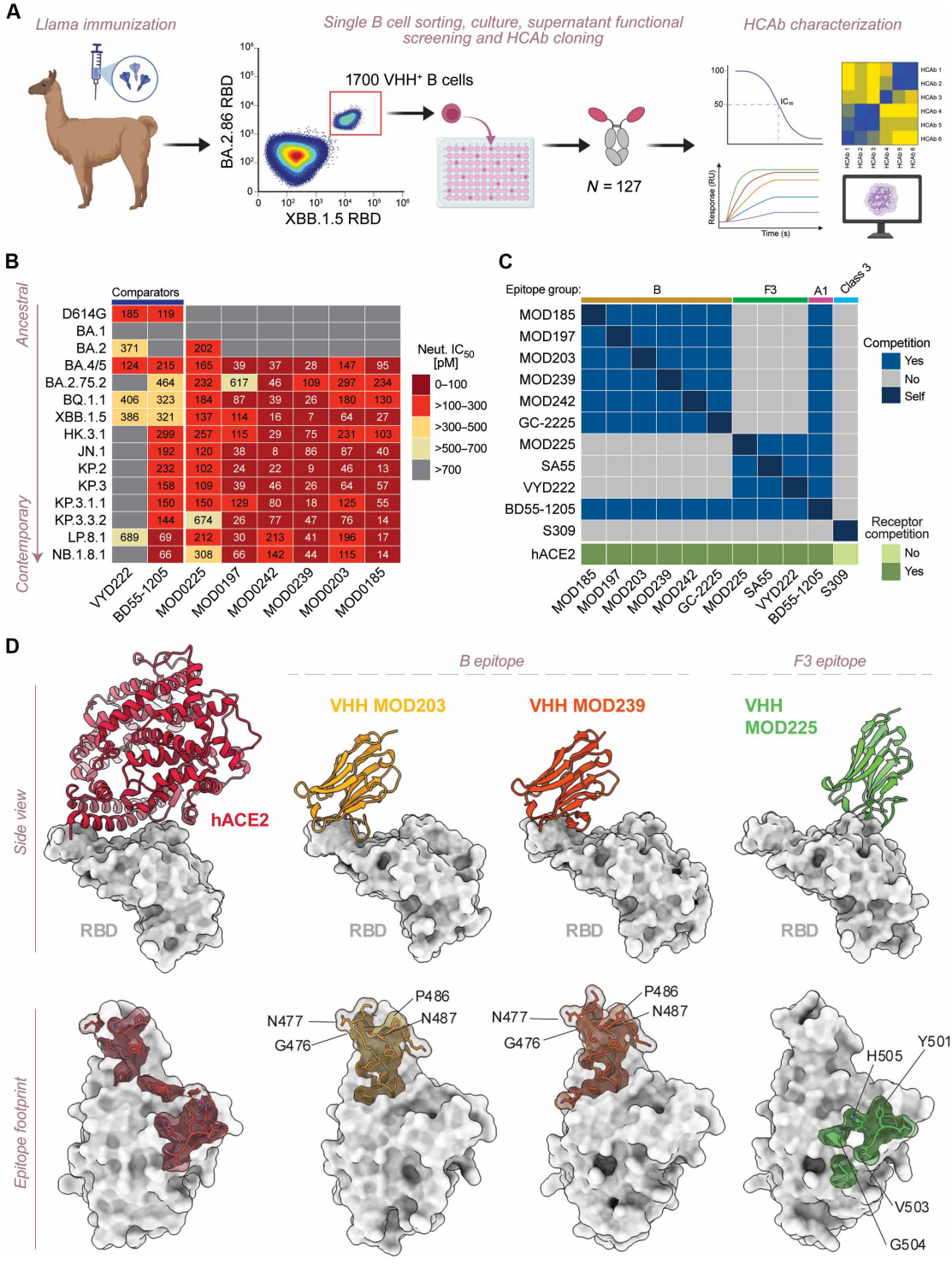


Fig. 1. Isolation of broad and potent anti–SARS-CoV-2 HCAbs from immunized llamas. (**A**) Overview of the llama immunization and HCAb discovery workflow, $n = 3$ animals; experimental workflow schematic was prepared with BioRender. (**B**) Heatmap showing the neutralization (Neut.) IC_{50} values of six lead llama-derived HCAbs (MOD225, MOD197, MOD242, MOD239, MOD203, and MOD185) and reference IgGs VYD222 and BD55-1205 (*8*, *19*) against SARS-CoV-2 variants spanning ancestral (D614G) to recently emerged, contemporary variants. (**C**) Surface plasmon resonance–based epitope binning of HCAbs using benchmark antibodies targeting defined RBD epitopes: GC-2225 (epitope B), BD55-1205 (epitope A1), VYD222 and SA55 (epitope F3), and S309 (class 3) (*47*). Blue indicates complete competition (binding response = 0), and gray indicates partial or no competition. Self-competition is shown in navy blue. hACE2 receptor competition for binding to RBD is indicated in green. (**D**) Crystal structures of KP.3 RBD bound to VHHs MOD203 (yellow), MOD239 (orange), and MOD225 (green). Top: overall binding orientation; bottom: corresponding footprints mapped onto the RBD surface. Residues forming key contacts are highlighted. The structure of KP.3 RBD bound to ACE2 (PDB: 9IUP; red) is shown for comparison.

Downloaded from https://www.science.org at Cambridge University on October 18, 2026

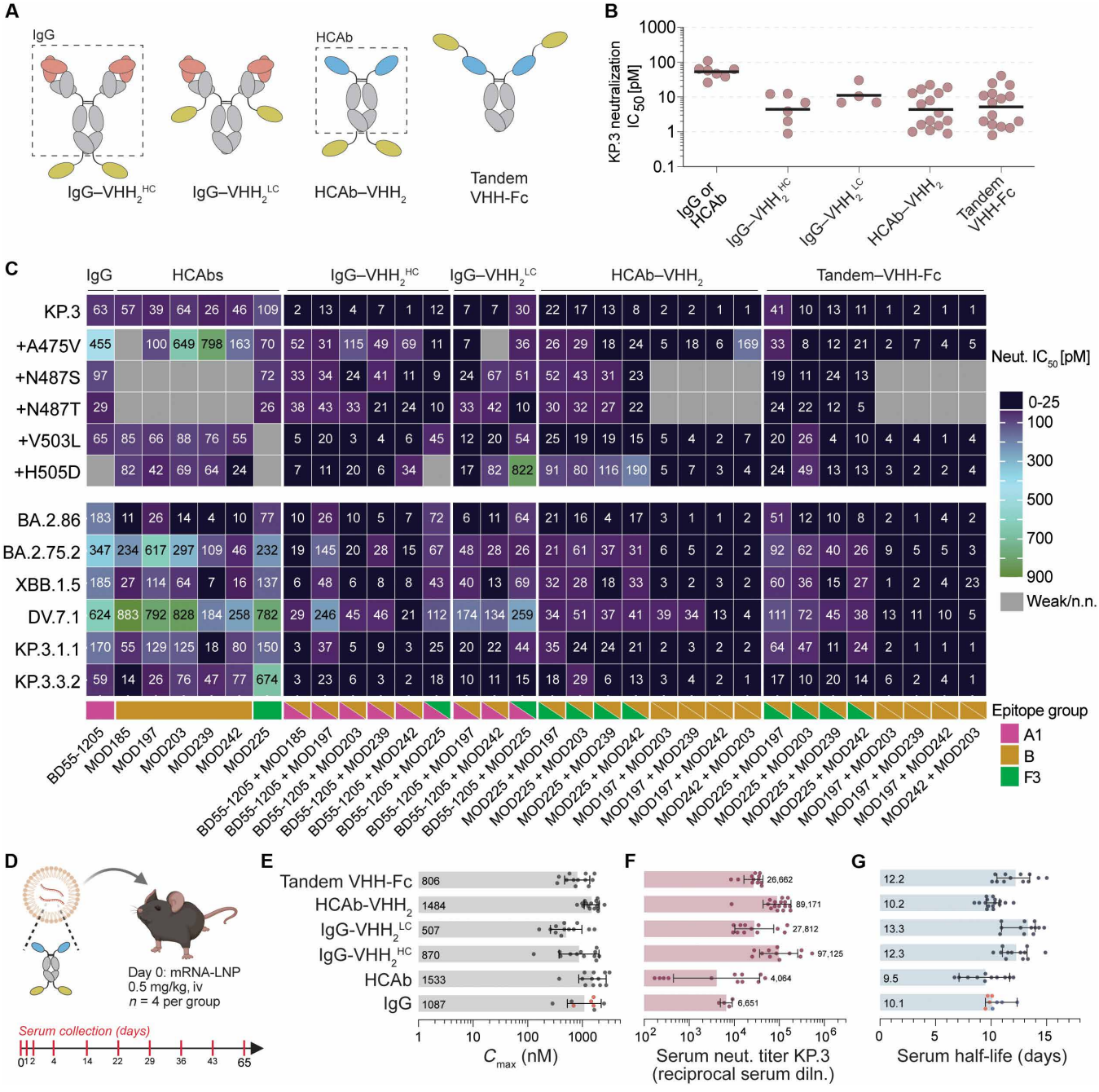


Fig. 2. bsAbs exhibit enhanced neutralization potency and breadth in vitro and in vivo. (**A**) Domain architectures of the four bsAb formats evaluated: IgG-VHH$_2^{HC}$ (VHH domain fusion to the C terminus of the HC), IgG-VHH$_2^{LC}$ (VHH domain fusion to the C terminus of the LC), HCAb-VHH$_2$, and tandem VHH-Fc. Dashed boxes indicate the regions corresponding to parental IgGs or HCAbs. (**B**) Neutralization potency (IC_{50}) of parental antibodies and bsAbs against SARS-CoV-2 KP.3 pseudovirus. Black bars indicate geometric mean. (**C**) Neutralization IC_{50} values against KP.3 escape mutants and a selection of SARS-CoV-2 variants. Multicolor bar below the heatmap indicates RBD epitope assignments for parental antibodies and bsAbs. n.n., nonneutralizing. (**D**) Study design for in vivo expression analysis of mRNA-encoded parental monospecific antibodies and bsAbs in Tg32-SCID mice ($n = 4$ per group). mRNA-LNPs were administered intravenously (iv) at a dose of 0.5 mg/kg, and serum was collected at the indicated time points for analyses shown in (E) to (G). (**E**) Peak serum concentrations of the indicated mRNA-encoded antibodies, as determined by ELISA (geometric mean ± SD). (**F**) Peak serum neutralization titers against KP.3 pseudovirus (geometric mean ± SD); diln., dilution. (**G**) Serum half-lives (median with 95% CI). Red circles in (E) and (G) denote CHKV-24/mRNA-1944 (clinical benchmark). Numbers in or next to bars indicate geometric means [(E) and (F)] or median (G). Each point represents one animal; animals receiving antibodies of the same format were grouped for analysis.

Downloaded from https://www.science.org at Cambridge University on October 18, 2026

mRNA-delivered bsAbs achieve high serum neutralizing titers and favorable pharmacokinetics in human FcRn–expressing mice

We next investigated whether mRNA-LNP delivery could bypass manufacturing and formulation constraints associated with recombinant production of bsAb cocktails by enabling high in vivo expression titers and preserved functional activity. Thirteen mRNA-encoded bsAbs and four parental control antibodies were selected for in vivo expression studies in human neonatal Fc receptor (FcRn)–expressing Tg32-SCID mice (Fig. 2D; fig. S4, A and B; and table S2). An mRNA-encoded anti-chikungunya IgG (CHKV-24/mRNA-1944), previously shown to have a serum half-life of ~69 days in a phase 1 clinical trial, was also included as an in vivo expression and half-life benchmark (*22*). All antibodies contained either the Met^{428}→Leu (M428L)/Asn^{434}→Ala (N434A) (LA; bsAbs and parental controls) or M428L/Asn^{434}→Ser (N434S) (LS; CHKV-24/mRNA-1944) Fc modification to extend serum half-life (*23*, *24*). Forty-eight to 96 hours after intravenous delivery, the bsAbs reached peak serum concentrations (C_{max}) ranging from 459 to 2020 nM (geomean: 1061 nM), with most achieving peak concentrations comparable to those of the parental HCAbs (geomean: 1533 nM), BD55-1205 IgG (geomean: 930 nM), and CHKV-24/mRNA-1944 IgG control (geomean: 1269 nM) (Fig. 2E and fig. S4, A and B). Owing to their high neutralization potency, the in vivo delivered bsAbs exhibited 11-fold higher geometric mean peak serum neutralizing titers against KP.3 compared with monospecific HCAb/IgG antibodies (Fig. 2F). Most of the bsAbs also displayed comparable or superior pharmacokinetics relative to the parental antibodies and CHKV-24/mRNA-1944, with median serum half-lives ranging from 9.5 to 13.9 days, demonstrating that bsAb engineering did not negatively affect FcRn-mediated recycling or accelerate clearance through other nonspecific mechanisms (Fig. 2G and fig. S4, A and B). Together, these results demonstrate that mRNA-delivered bsAbs can achieve potent and durable serum neutralizing antibody titers in a humanized FcRn mouse.

Fc engineering enables multiplexed delivery of mRNA-encoded bsAb combinations with cognate HC pairing

We next explored the feasibility of delivering combinations of mRNA-encoded bsAbs with orthogonal escape profiles to further expand serum neutralization breadth and reduce the risk of viral escape. Although mRNA-LNP technology is well suited for multiplexed delivery of biotherapeutic proteins, in vivo expression of antibodies can result in mispairing of IgG HCs and LCs, potentially generating nonfunctional antibody species (*25*). VHH-based bsAb formats eliminate the risk of LC mispairing; however, preventing HC mispairing requires Fc engineering strategies that enforce homodimerization. Therefore, we used structure-based computational engineering to develop multiple orthogonal Fc homodimerization modifications that would enable mRNA delivery of several bsAbs with cognate chain pairing, each encoded by a single HC mRNA.

Because the Fc CH3-CH3 interaction is the principal driver of Fc dimerization, we focused our Fc homodimerization engineering strategy on the CH3 domain interface. This region contains a central hydrophobic core surrounded by charged residues that mediate electrostatic interactions essential for dimer formation (*26*) (Fig. 3A). Using the crystal structure of human IgG1 Fc [Protein Data Bank (PDB) ID: 4W4N] as a template, we designed and tested several orthogonal homodimerization strategies based on two complementary approaches: steric complementarity ["knobs-into-holes"–like (*27*)] and electrostatic steering. For the steric design, a "knob" was introduced by replacing threonine at position 366 with the bulkier isoleucine (T366I), whereas the corresponding "hole" was introduced by substituting bulky residues at positions 368 and 407 [Leu^{368}→Ala (L368A) and Tyr^{407}→Val (Y407V)] with smaller amino acids. This combination of mutations favors specific homodimer formation while disfavoring heterodimerization and is henceforth abbreviated Fc^{IAV} (Fig. 3B). For the electrostatic steering approach, we introduced two distinct charge-swap modifications at the CH3 interface. The first set of mutations—Asp^{399}→Lys (D399K), Lys^{409}→Asp (K409D), and Lys^{392}→Gln (K392Q)—was designed to preserve favorable salt bridges in homodimers and generate charge repulsion in heterodimers. In the wild-type (WT) dimer, D399 forms a salt bridge with K409. Swapping these residues (D399K and K409D) maintains favorable interactions in the homodimer but leads to repulsive interactions in the heterodimer (between D399 and D409 on one chain and between D399K and K409/K392 on the other), thereby biasing the interface toward homodimerization (Fig. 3C). This set of mutations is referred to as Fc^{KDQ}. The second type of charge mutations, Ser^{364}→Lys (S364K) and Lys^{370}→Asp (K370D), similarly leverages salt-bridge formation in the homodimer while introducing repulsive interactions in heterodimer and is herein abbreviated as Fc^{KD} (Fig. 3D). Together, these three sets of engineered mutations—(i) Fc^{IAV}, (ii) Fc^{KDQ}, and (iii) Fc^{KD}—combine steric and electrostatic design principles to bias the CH3 domain interface toward Fc homodimer formation.

To evaluate whether the three Fc homodimerization designs promoted cognate HC pairing in vivo in the presence of wild-type Fc (Fc^{WT}), we carried out a pairwise codelivery assessment by administering mRNA-LNPs encoding two prototype HCAbs (one bearing the designed Fc and the other Fc^{WT}) into C57BL/6 mice at a 1:1 ratio (Fig. 3E and table S2). Liquid chromatography–mass spectrometry (LC-MS) analysis of pairing efficiency revealed predominantly chimeric species when two HCAbs were codelivered using Fc^{WT}, whereas Fc homodimerization mutations drove highly specific preferential pairing of the desired HCAbs, with minimal or undetectable chimera formation (Fig. 3, F to I). In an in vitro mRNA-LNP cotransfection experiment, codelivery of the prototypic HCAbs bearing the three homodimerization designs together with Fc^{WT} resulted in the generation of four cognate homodimer species with minimal chimera formation (fig. S5). Last, we assessed the efficiency of cognate chain pairing in the context of mRNA-encoded bsAb combinations by performing mammalian cell transfections with mRNA-LNPs encoding three bsAbs bearing either Fc^{WT} or Fcs containing homodimerization modifications (Fig. 3J). Intact MS analysis confirmed a reduction in undesired chimeric bsAb species in the codelivery condition containing orthogonal homodimerization mutations (Fc^{WT} + Fc^{KDQ} + Fc^{KD}) compared with Fc^{WT} (Fig. 3J). In summary, we engineered a set of Fc homodimerization modifications that enable codelivery of up to four mRNA-encoded antibodies with cognate HC pairing.

mRNA-delivered bsAb combinations enhance serum neutralization breadth in mouse models

We next evaluated whether multiplexed delivery of three Fc-engineered bsAbs would provide enhanced serum neutralization breadth and potency relative to individual bsAbs, parental monospecific antibodies, and combinations of parental antibodies. The

Downloaded from https://www.science.org at Cambridge University on October 18, 2026

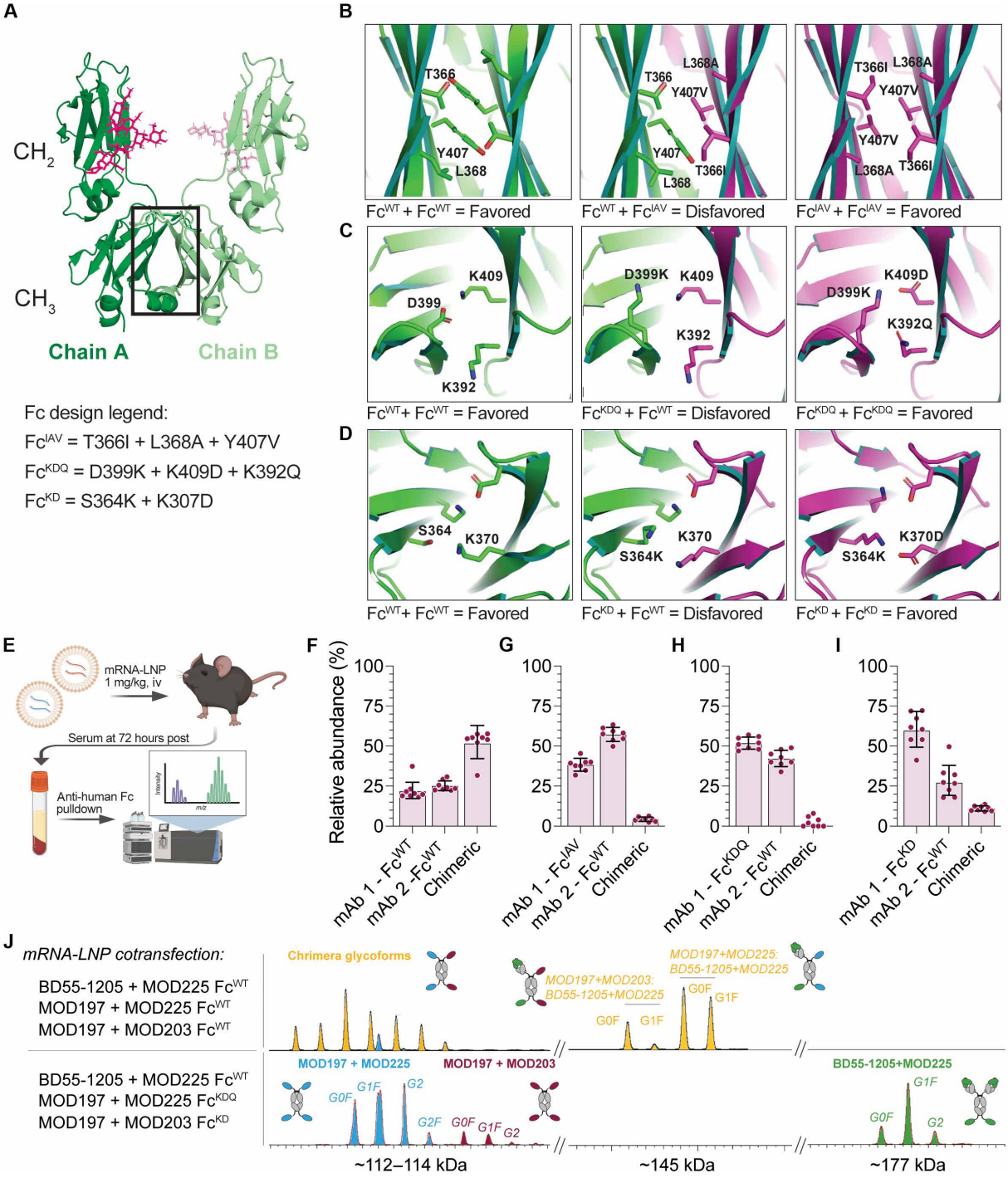


Fig. 3. Engineered Fc mutations enforce cognate HC pairing to enable delivery of mRNA-encoded bsAb combinations. (**A**) IgG1 Fc structure (PDB: 4W4N) highlighting the CH3-CH3 interface (black box) and designed homodimerization modifications. (**B** to **D**) Cartoon representations of homodimerization mutations: (B) steric complementarity mutations (Fc^{IAV} = T366I, L368A, and Y407V), (C) electrostatic steering mutations set 1 (Fc^{KDQ} = D399K, K409D, and K392Q), and (D) electrostatic steering mutations set 2 (Fc^{KD} = S364K and K370D). Designed homodimerization mutations are illustrated in pink, and Fc^{WT} is shown in green. Favored homodimers and disfavored heterodimers are indicated. (**E**) C57BL/6 mice ($n = 4$ animals per group) were dosed intravenously with mRNA-LNPs (1 mg/kg) containing a 1:1 mixture of mRNAs encoding the indicated antibodies, and serum collected at 72 hours was analyzed by MS. (**F** to **I**) MS analysis showing relative serum abundance of mAb-1 homodimer, mAb-2 homodimer, and mAb-1/2 heterodimer (chimeric) after in vivo codelivery of mRNA-encoded mAbs containing either both Fc^{WT} (F) or the following Fc homodimerization mutations: Fc^{IAV} + Fc^{WT} (G), Fc^{KDQ} + Fc^{WT} (H), and Fc^{KD} + Fc^{WT} (I). Data are presented as geometric means with SD. (**J**) In vitro transfection of Expi293 cells with mRNA-LNPs encoding the three indicated bsAbs with or without Fc homodimerization mutations. Antibodies were analyzed by intact MS to quantify cognate chain pairing efficiency. Labels above deconvoluted mass peaks indicate assigned antibody species and, where shown, distinct Fc-associated glycoforms; glycoform-labeled peaks represent the same underlying cognate or chimeric pairing species carrying different glycan compositions.

Downloaded from https://www.science.org at Cambridge University on October 18, 2026

selected triple bsAb combination incorporated binding domains from antibodies targeting the A1, F3, and B epitopes to maximize epitope diversity, with individual bsAbs selected to prioritize either breadth (e.g., BD55-1205/MOD225 IgG-VHH_2^{HC}) or potency (e.g., MOD197/MOD203 HCAb-VHH_2) (Fig. 4A). mRNA-LNPs encoding parental monospecific antibodies, individual bsAbs, a four-monospecific antibody combination, or a three-bsAb combination were delivered to groups of C57BL/6 mice at a matched total dose of 1 mg/kg of mRNA-LNP (combinations mixed in 1:1 ratios), and blood was collected at 48 and 72 hours after administration to measure serum neutralizing activity and cognate Fc pairing efficiency, respectively (fig. S6A and table S2).

To characterize the breadth of serum neutralizing activity across treatment groups, we evaluated titers against representative historical variants (ancestral SARS-CoV-2 D614G and BA.2), a contemporary variant (KP.3), selected KP.3 escape variants (H505D and N487T), and the recently emerged BA.3.2.2 variant, which contains 68 mutations relative to JN.1 (Fig. 4B). Neutralizing activity varied across the parental-antibody and individual bsAb groups, with each group showing low or undetectable titers against at least one variant. The three-bsAb combination was the only group with geometric mean serum neutralizing titers greater than 1:9000 against all six variants tested, with titers ranging from 9846 against D614G to 553,683 against KP.3 (Fig. 4B and fig. S6B). The combination of four

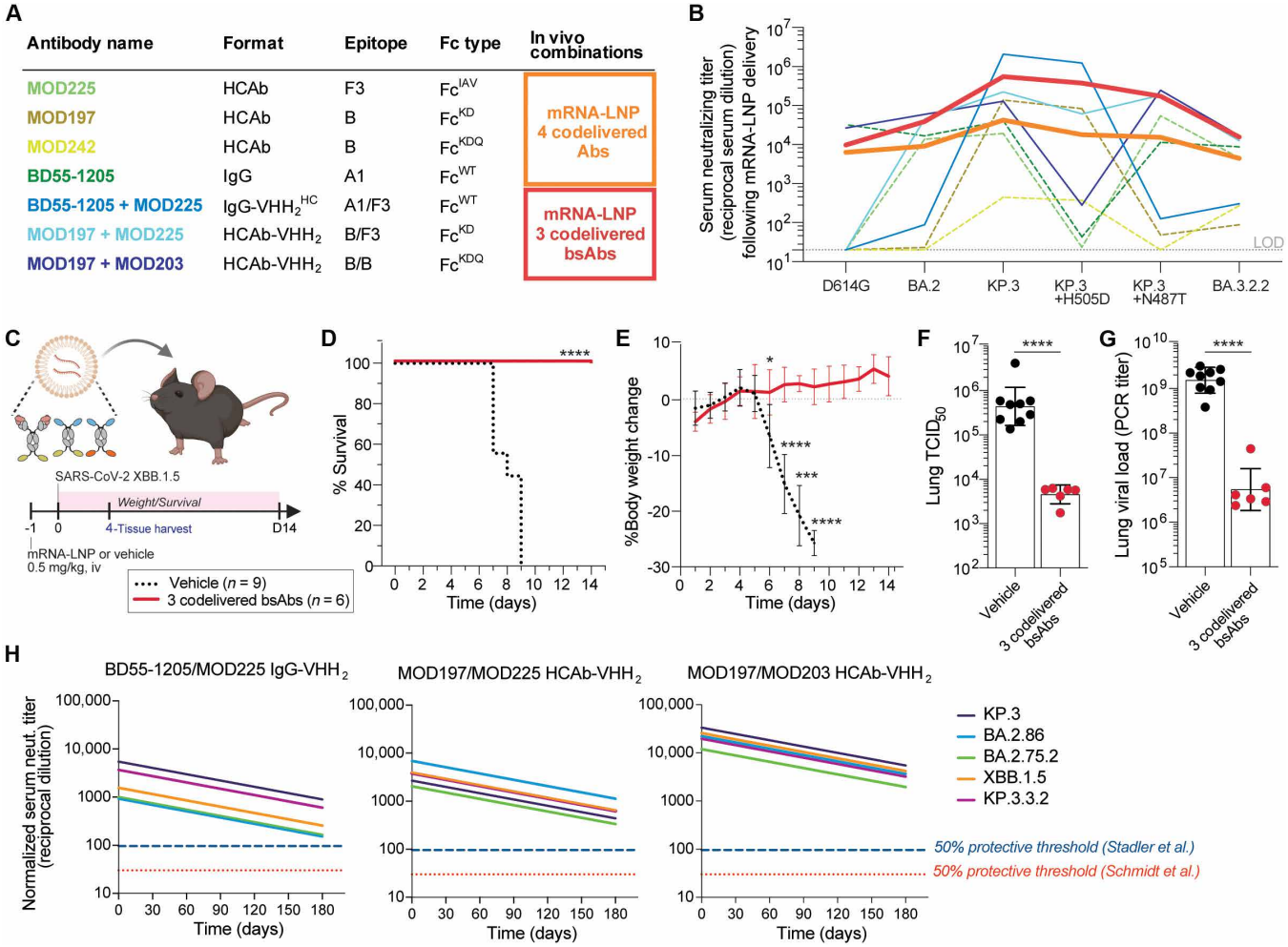


Fig. 4. mRNA-delivered bsAb combinations provide broad serum neutralization and prophylactic protection in mice and are projected to sustain protective titers in humans. (**A**) Antibody constructs and in vivo treatment groups evaluated in C57BL/6 mice. Animals received intravenous mRNA-LNP (1 mg/kg) encoding parental antibodies, bsAbs, four monospecific antibodies, or three Fc-engineered bsAbs. (**B**) Serum neutralizing titers against the indicated SARS-CoV-2 variants at 48 hours. Colors correspond to the constructs shown in (A), denoting parental antibodies (shades of green), individual bsAbs (shades of blue), the four-antibody combination (orange), and the three-bsAb combination (red); LOD, limit of detection. (**C**) Prophylactic challenge study design in hACE2 AC70 mice. Animals received 0.5 mg/kg of mRNA-LNPs encoding a three-bsAb combination or vehicle 24 hours before intranasal challenge with 1.96×10^4 PFU XBB.1.5. (**D**) Survival analysis for treated (red solid line) versus control (black dotted line) mice. Survival curves were compared by log-rank (Mantel-Cox) test ($P < 0.0001$). (**E**) Body weight changes (mean ± SD, $n = 6$ to 9 mice per group) in treated (red solid line) versus control (black dotted line) mice. Groups were compared over days 1 to 9 by two-way mixed-effects model with Holm-Šidák's multiple-comparisons test; $^*P < 0.05$, $^{***}P < 0.001$, and $^{****}P < 0.0001$. (**F** and **G**) Lung infectious virus titer by 50% tissue culture infectious dose $TCID_{50}$ assay (F) and viral subgenomic RNA by RT-qPCR (G) at day 4 (geometric mean ± SD); data were analyzed by two-tailed unpaired *t* tests, $^{****}P < 0.0001$. (**H**) Human serum neutralizing titer projections for three lead bsAbs, calculated using the 10 μg/ml peak concentration and 69-day half-life reported for mRNA-1944 and variant-specific IC_{50} values (*22*, *23*). Dashed lines indicate published 50% protective thresholds (*23*, *32*).

Downloaded from https://www.science.org at Cambridge University on October 18, 2026

parental IgGs and HCAbs also increased neutralization breadth relative to the individual parental antibodies and bsAbs; however, titers against KP.3 and its H505D and N487T escape variants were 11- to 21-fold lower than those achieved with the three-bsAb combination.

To determine the impact of enforced cognate chain pairing on serum neutralizing activity, we also compared the three-bsAb combination containing Fc homodimerization mutations with an otherwise matched three-bsAb combination containing Fc^{WT} domains, which permits noncognate chain pairing after mRNA delivery. Serum neutralizing titers were measured against KP.3 and the KP.3 escape variant H505D, which showed resistance to a subset of the antibodies in the bsAb combination (Fig. 2C and fig. S6C). The three-bsAb combination containing homodimerization mutations produced higher serum neutralizing titers across KP.3 and KP.3 + H505D than the Fc^{WT} comparator (Friedman test, $P = 0.0024$; fig. S6C), consistent with enhanced functional activity resulting from cognate chain pairing. The relatively high serum neutralizing titers observed with the Fc^{WT} bsAb combination likely reflect the high intrinsic affinity of the individual Fab arms, reducing dependence on avidity-mediated neutralization, as previously described (*28*).

An mRNA-encoded three-bsAb combination protects against SARS-CoV-2 XBB.1.5 challenge in hACE2 transgenic mice

We next investigated whether the mRNA-encoded three-bsAb combination could provide prophylactic protection against SARS-CoV-2 XBB.1.5 disease in hACE2 AC70 transgenic mice (*29*–*31*). XBB.1.5 was selected for this study because it produced a more reproducible disease phenotype in this mouse model compared with post-JN.1 variants. mRNA-LNPs encoding the three-bsAb combination were prophylactically administered to mice at 0.5 mg/kg intravenously (iv) 24 hours before intranasal challenge with SARS-CoV-2 XBB.1.5 [1.96×10^4 plaque-forming units (PFU)] (Fig. 4C). This mRNA-LNP dose falls within the range previously evaluated in the CHKV-24/mRNA-1944 clinical study, in which mRNA-LNP administration was well tolerated and supported repeat dosing (*22*). Mice were monitored daily for weight loss, and a subset was euthanized at day 4 after infection to allow for measurement of virus replication in the lungs. Infection of vehicle-treated hACE2 AC70 mice with SARS-CoV-2 XBB.1.5 resulted in weight loss after day 5, resulting in complete mortality by day 9 after infection. In contrast, all mice treated prophylactically with the three-bsAb combination survived without weight loss (log-rank Mantel-Cox test, $P < 0.0001$; two-way mixed-effects model with Holm-Šidák's multiple-comparisons test, $P < 0.0001$; Fig. 4, D and E). Furthermore, the three-bsAb combination reduced infectious viral titers in the lungs and viral RNA levels at 4 days after infection (two-tailed unpaired *t* tests, $P < 0.0001$ for both comparisons; Fig. 4, F and G). We conclude that mRNA-delivered bsAb combinations enhance serum cross-neutralizing activity and provide robust prophylactic protection against SARS-CoV-2 challenge in hACE2 transgenic mice.

Clinical benchmark–informed exposure projections suggest durable prophylactic protection in humans after mRNA delivery of bsAbs

Because serum concentrations of mRNA-delivered antibodies in mice may exceed those achieved in humans, we performed a clinical benchmark–informed exposure analysis to estimate human serum neutralizing titers using the clinical data reported for CHKV-24/mRNA-1944 (*22*). The mRNA-encoded bsAbs evaluated in this study achieved peak serum concentrations in Tg32 mice that were comparable to those of CHKV-24/mRNA-1944 (Fig. 2E), and therefore, we used the reported human peak serum concentration of mRNA-1944 at the 0.6 mg/kg dose (10 μg/ml) as a clinically relevant estimate of achievable peak exposure (*22*). For each of the three lead mRNA-encoded bsAbs, we calculated normalized peak serum neutralizing titers by dividing this estimated peak serum concentration by the variant-specific neutralization IC_{50} values for each bsAb (Fig. 2C) (*23*, *32*). Because the lead bsAbs also showed serum half-lives in human FcRn mice that were similar to the mRNA-1944 benchmark, we projected serum titer decay using the 69-day serum half-life observed for mRNA-1944 in the clinical study. On the basis of these assumptions, all three mRNA-encoded bsAbs achieved predicted peak serum neutralizing titers of ≥1:900 and remained above 1:100 at 6 months (Fig. 4H). Published SARS-CoV-2 mAb correlates of protection analyses have shown that ~50% protection against symptomatic COVID-19 is associated with serum neutralizing titers in the range of ~1:30 to 1:100 (*8*, *23*, *32*). Thus, although this analysis is benchmark based and depends on extrapolation from mRNA-1944 clinical exposure and half-life data, it suggests that the mRNA-encoded bsAbs described here could maintain protective serum neutralizing activity for at least 6 months in humans.

DISCUSSION

The long-term effectiveness of antiviral vaccines stems in part from their ability to induce polyclonal antibody responses that recognize a diversity of protective epitopes, collectively limiting viral escape from immune pressure. In contrast with vaccines, antiviral IgG monotherapies and two-mAb combinations have shown greater susceptibility to the emergence of resistance because of their restricted epitope coverage (*6*, *33*–*35*). Although prior studies have sought to overcome this challenge through the development of bsAbs, many of these molecules remain vulnerable to certain escape variants (*14*–*16*, *36*), and clinical translation has been constrained by the complexity of manufacturing multivalent antibody products. In this study, we addressed these limitations by integrating antibody engineering with mRNA platform technology to enable in vivo expression of multiple anti–SARS-CoV-2 bsAbs, resulting in highly potent serum neutralization and enhanced resistance to viral escape relative to individual bsAbs or combinations of parental molecules.

To isolate broadly reactive binding domains for bsAb engineering, we used a large-scale functional screening approach to evaluate more than 500 llama B cell–derived supernatants for binding and neutralizing activity against a panel of SARS-CoV-2 variants. Although high-throughput B cell isolation platforms have been widely applied for human IgG discovery, our study represents a large-scale functional screen designed to comprehensively interrogate camelid HCAb repertoires. This approach yielded multiple HCAbs with cross-neutralizing activity spanning historical and contemporary Omicron subvariants, and incorporation of these VHH domains into bsAbs conferred substantial gains in breadth, potency, and resistance to viral escape. The most potent bsAbs achieved pseudovirus neutralization IC_{50} values in the low picomolar range, representing 10- to 100-fold improvements in potency against post-JN.1 variants relative to the clinically approved IgG monotherapy VYD222 (*8*).

The majority of mRNA-encoded bsAbs exhibited comparable or superior peak serum concentrations and pharmacokinetics in

Downloaded from https://www.science.org at Cambridge University on October 18, 2026

hFcRn-expressing mice relative to the conventional IgG and HCAb antibodies, suggesting that in vivo mRNA delivery can overcome the expression and stability limitations often associated with recombinant production of multivalent antibody formats (*13*). Furthermore, owing to their increased potency, the bsAbs achieved more than 10-fold higher peak serum neutralizing titers against KP.3 than the corresponding parental antibodies while maintaining similar serum expression kinetics.

To further enhance resilience to viral escape through multiplexed delivery of mRNA-encoded bsAbs, we used structure-guided engineering to develop Fc homodimerization modifications that enforce cognate HC pairing of up to four codelivered antibodies, each encoded by a single mRNA. The Fc mutations described here are distinct from the asymmetric heterodimerization modifications commonly used to generate IgG-like bsAbs with dual specificities (*26*, *27*), and their symmetric design circumvents the complexity of chain expression balancing and increased dose requirements. In vivo expression of an Fc-engineered triple bsAb combination resulted in higher serum neutralizing titers and improved variant coverage relative to individual bsAbs, combinations of parental antibodies, and combinations of non–Fc-engineered bsAbs, underscoring the potential for mRNA-encoded bsAb cocktails to counter the evolving SARS-CoV-2 landscape. Moreover, given the recent shift toward immunobridging strategies for regulatory approval of updated SARS-CoV-2 antibody therapeutics (*8*), mRNA-delivered bsAbs could accelerate the clinical development process further by enabling rapid manufacturing of optimized antibodies tailored to emerging variants.

More broadly, the approach described here provides a modular framework for the expression of oligoclonal antibody combinations through a genetically encoded therapeutic. Beyond SARS-CoV-2, this concept could be applied to other antigenically variable viruses that require coverage of many different circulating strains or used to confer broad protection against divergent cocirculating pathogens. For example, clinical studies of the anti–HIV-1 bnAb VRC01 demonstrated protection against susceptible HIV isolates but no reduction in overall HIV-1 acquisition because of the high prevalence of circulating escape variants (*37*). Improved prophylactic efficacy could be achieved by coexpressing multiple mRNA-encoded bnAbs targeting nonoverlapping epitopes to broaden coverage of global circulating isolates. Similarly, this approach could be applied to influenza virus, where antigenic diversity and immune imprinting can limit durable vaccine efficacy (*38*), and could also be extended to mRNA delivery of multiple bsAbs targeting cocirculating respiratory viruses (e.g., respiratory syncytial virus, influenza virus, and SARS-CoV-2). Enforced Fc homodimerization may be especially important in the latter setting because mispairing among antibodies directed against distinct viral antigens will result in a complete loss of bivalent recognition (*39*). Last, mRNA-encoded antibody combinations could also be used in other therapeutic areas where breadth, resistance to escape, or multitarget engagement is advantageous, such as broad-spectrum antivenoms to treat snakebite envenoming or simultaneous targeting of multiple tumor-associated antigens, immune checkpoints, or other disease-relevant pathways in cancer and autoimmunity.

There are several limitations to this study. First, the engineered Fc modifications introduce nongermline residues and therefore carry a theoretical risk of creating immunogenic neoepitopes. Although available nonclinical and clinical experience with engineered IgG-like bsAbs suggest that Fc pairing mutations are not inherently associated with high immunogenicity risk (*40*), the immunogenicity of the homodimerization modifications described here will require assessment in future clinical studies. Second, we did not assess the therapeutic efficacy of the mRNA-encoded bsAb combination in a postinfection challenge model. We focused on preexposure prophylaxis because this setting has an established correlate of protection, addresses a high unmet need in immunocompromised individuals, and is better supported by clinical evidence compared with therapeutic settings (*41*–*43*). Nevertheless, postexposure therapeutic activity remains an important area for future investigation. Last, we were unable to directly evaluate potential interference among codelivered antibodies targeting the same antigen because of technical limitations. However, previous studies have shown limited to no interference in expression of mRNA-delivered antibody combinations (*44*), and the multiplexed antibody cocktail retained broad neutralizing activity against viral variants for which individual bsAbs showed reduced or lost activity, which would be unlikely in the setting of substantial expression interference.

In summary, our study establishes a generalizable framework for the integration of high-throughput VHH discovery, structure-guided Fc engineering, and mRNA-based multiplexed delivery of antibodies to combat antigenically variable viruses. More broadly, this platform may have applications in other therapeutic areas in which broad antigen coverage, resistance to escape, or simultaneous engagement of multiple disease-associated targets is desirable.

MATERIALS AND METHODS

Study design

The objective of this study was to develop broadly neutralizing, mRNA-encoded bsAbs against SARS-CoV-2 and determine whether engineered Fc homodimerization modifications could enable multiplexed in vivo expression of bsAb combinations with cognate HC pairing. Antibodies isolated from immunized llamas were characterized by binding and neutralization assays, epitope mapping, viral escape analysis, and x-ray crystallography and were used to generate bsAbs in four molecular formats. mRNA-LNP delivery was evaluated in Tg32-SCID and C57BL/6 mice to assess serum antibody expression, pharmacokinetics, neutralizing activity, and HC pairing. Prophylactic efficacy was evaluated in hACE2 AC70 transgenic mice challenged with SARS-CoV-2 XBB.1.5 by measuring survival, body weight, infectious lung viral titers, and lung viral RNA. Animals were randomized to experimental groups. Animal studies were conducted under Institutional Animal Care and Use Committee (IACUC)–approved protocols and in accordance with applicable animal-welfare regulations.

Ethics statement

All animal studies were conducted under an IACUC–approved protocol (IACUC 23-07-016) in compliance with the Animal Welfare Act, Public Health Service policy, and other applicable state and city public laws and regulations. Animal studies were designed and executed following the guidelines from the *Guide for the Care and Use of Laboratory Animals*, 8th edition. Llama procedures were performed at Lampire Biological Laboratories Inc., under IACUC–approved protocols. All in-life animal handling of the transgenic hACE-2AC70 mice occurred at BIOQUAL Inc. The animal study was conducted by BIOQUAL Inc. under an IACUC protocol (no. 25-046, approved April 2025).

Downloaded from https://www.science.org at Cambridge University on October 18, 2026

Llama immunization and PBMC and plasma isolation

Llamas were primed with 100 μg of mRNA-LNPs encoding XBB.1.5 S-2P administered intramuscularly. Subsequent boosts with recombinant proteins were delivered subcutaneously in the axillary region areas or along the dorsal flank in the presence of incomplete Freund's adjuvant (IFA). To diversify anti-RBD VHH responses, llamas received sequential boosts with 1 mg of recombinant XBB.1.5 spike protein (day 21), XBB.1.5-RBD (day 28), SARS1-RBD (day 35), and BA.2.86-RBD (day 56). Whole blood was collected on day 63 after prime immunization. Peripheral blood mononuclear cells (PBMCs) were isolated using SepMate-50 tubes (Stemcell, 85450), washed with phosphate-buffered saline (PBS), and cryopreserved in freezing medium containing dimethyl sulfoxide (Lampire Biological Laboratories, 7572001). PBMCs were stored in liquid nitrogen until thawing for B cell isolation experiments.

Recombinant protein expression and purification

Recombinant SARS-CoV-2 RBD proteins were expressed by encoding sequences in a pcDNA3.4 expression vector (GeneImmune) and transiently expressed in Expi293F cells using Turbo293 (Speed Biosystems, PXX1006). Conditioned medium collected 4 to 5 days after transfection were clarified by centrifugation using 0.22-μm filtration and applied to a Strep-Tactin XT 4Flow column (IBA Lifesciences, 2-5013-001) equilibrated in PBS. Bound protein was eluted with biotin. Eluates were concentrated using 10-kDa Amicon Ultra centrifugal filters (Millipore Sigma, UFC5010) to prepare for size exclusion chromatography (SEC), then polished and buffer exchanged by SEC on a Superdex 200 Increase column equilibrated in PBS (pH 7.4). Monomeric fractions were pooled, sterile filtered (0.22 μm), quantified by A280, and stored at −80°C.

Enzyme-linked immunosorbent assay

To determine anti-RBD serum titers after llama immunization, enzyme-linked immunosorbent assay (ELISA) plates (Corning, 3997) were coated with SARS-CoV-2 XBB.1.5-RBD (1 μg/ml; Acro-Biosystems, SPD-C5242) diluted in PBS and incubated overnight at 4°C. Plates were washed with wash buffer (PBS/0.05% Tween 20) and blocked with SuperBlock buffer (Thermo Fisher Scientific, 37515). Serial dilutions of llama serum, starting at 1:10 dilution, were added to the plates. Plates were washed and incubated with peroxidase-conjugated rabbit anti-camelid VHH (GenScript, A02016) or goat anti-llama IgG (H + L) (Southern Biotech, 6045-05) at room temperature for 90 min. Plates were washed and developed using 3,3′,5,5′-tetramethylbenzidine (TMB) peroxidase substrate (SeraCare, 5120–0050), and the reaction was stopped with TMB stop solution (Fisher, 50-674-44). Absorbance was measured at 450 nm and analyzed using a four-parameter logistic curve (Prism v.10).

Antibody concentrations in mouse serum were determined by coating ELISA plates (Thermo Fisher Scientific, 439454) with goat anti-human IgG Fc (2 μg/ml; Fortis Life Sciences, A80-104) diluted in PBS and incubated overnight at 4°C. Plates were washed with wash buffer (PBS with 0.05% Tween 20) and blocked with SuperBlock buffer (Thermo Fisher Scientific, 37515). Serial dilutions of mouse serum (starting at 1:30 dilution) or an equivalent recombinant protein standard (starting at 1 μg/ml) were added in assay diluent (PBS with 5% goat serum and 0.05% Tween 20). Plates were washed and incubated with peroxidase-conjugated goat anti-human IgG (Southern Biotech, 2040-05) at room temperature for 1 hour. Plates were washed and developed using TMB peroxidase substrate (SeraCare, 5120-0050), and the reaction was stopped with TMB stop solution (Fisher, 50-674-44). Absorbance was measured at 450 nm and analyzed using four-parameter nonlinear regression. Serum concentration was determined using the protein standard reference curve.

Flow cytometry analysis and single-cell sorting/culturing

Llama PBMCs were thawed and stained with 100 nM twin-strep tagged SARS-CoV-2 XBB.1.5 and BA.2.86 RBD-subdomain 1 (SD1) (a 1:1 mix), preincubated with Streptactin-phycoerythrin (PE) (IBA, 6-5000-001) or Streptactin-allophycocyanin (APC) (IBA, 6-5010-001), respectively, in a 2:1 ratio. Antigen-specific cells were enriched using anti-PE (Miltenyi, 130-048-801) and anti-APC (Miltenyi, 130-090-855) magnetic beads and separated using magnetic-activated cell sorting (MACS) LS columns (Miltenyi, 130-042-401). Enriched cells were stained using the following antibodies: anti-llama IgG-DyLight405 (Jackson ImmunoResearch, 128-475-160), anti-camelid VHH-FITC (GenScript, A02226–200), and Live/Dead near-infrared (NIR) (Thermo Fisher Scientific, L10119). VHH^+ B cells cross-reactive to both XBB.1.5 and BA.2.86 RBDs were single-cell sorted into 96-well U-bottom plates (Corning, 3799) containing irradiated Chinese hamster ovary (CHO)–CD40 ligand (CD40L) feeder cells, supplemented with IL-2 and IL-21 cytokines (produced at GenScript). CHO-CD40L cells were generated by transfecting CHO-K1 cells with alpaca CD40L open reading frame (plasmid produced at GenScript), using Lipofectamine 2000 (Thermo Fisher Scientific, 11668019), and selected/cultured using G418 (600 μg/ml; Gibco, 10131027). Cells were cultured for 14 days at 37°C. Supernatants were harvested for downstream screening and frozen at −20°C; remaining cells were frozen in lysis buffer (Invitrogen, A33562) and stored at −80°C.

Llama B cell culture supernatant ELISA and Luminex screening

Supernatants from cultured llama B cells were screened to determine VHH^+ B cell growth. ELISA plates (Corning, 3690) were coated with goat anti-alpaca IgG (1 μg/ml), subclass 2 + 3 (Jackson ImmunoResearch, 128-005-229), diluted in PBS, and incubated overnight at 4°C. Plates were washed with wash buffer (PBS containing 0.05% Tween 20) and subsequently blocked with SuperBlock buffer (Thermo Fisher Scientific, 37515) for 1 hour at room temperature. Supernatants were diluted 1:10 in blocking buffer and added to the plates in a single dilution. After washing, plates were incubated with peroxidase-conjugated rabbit anti-camelid VHH antibody (GenScript, A02016) for 90 min at room temperature. After additional washes, TMB peroxidase substrate (SeraCare, 5120-0050) was added for color development, and the reaction was stopped using TMB stop solution (Thermo Fisher Scientific, 50-0674-44). Absorbance was measured at 450 nm using a microplate reader. Wells were considered positive when the optical density (OD_{450}) exceeded twofold more than background (media only control). VHH^+ wells were subsequently selected and assessed for antigen-specific binding using a Luminex assay.

For Luminex assays, MagPlex microsphere beads (Luminex) were conjugated to RBD proteins from multiple SARS-CoV-2 variants [WT (D164G), Delta, BA.1, BA.2, BA.4/5, XBB.1.5, JD.1.1, BQ.1.1, HK.3.2, BA.2.86, JN.1, XCT.1] using a sulfo-*N*-hydroxysulfosuccinimide/1-ethyl-3-(3-dimethylaminopropyl)carbodiimide coupling reaction (Thermo Fisher Scientific, A35391 and 24510), at a concentration of 50 pmol protein per 1×10^6 beads. B cell culture supernatants were

Downloaded from https://www.science.org at Cambridge University on October 18, 2026

diluted 1:10 in assay buffer (Teknova, 20238) and incubated with 500 beads per well for each antigen tested. Bead-supernatant mixtures were added to a 384-well microplate (Greiner Bio-One, 781903) and incubated overnight at 4°C on a shaker.

After incubation, magnetic beads were washed four times with assay buffer using a plate magnet. Beads were then incubated with mouse anti-llama IgG2/3 antibody (Southern Biotech, 5880-01M) at 0.65 μg/ml in assay buffer for 1 hour at room temperature on a shaker. After washing, beads were incubated with PE-conjugated anti-mouse IgG (Southern Biotech, 1030-90) at 0.65 μg/ml in assay buffer for 30 min at room temperature on a shaker. Beads were then washed, resuspended in MagPlex Sheath Fluid (DiaSorin, 40-50021), and analyzed on a Luminex xMAP Intelliflex instrument. Data were analyzed by calculating the PE median fluorescence intensity (MFI) fold change relative to a medium-only negative control. A fold change of ≥10 was considered the threshold for a positive response.

In vitro neutralization assay

B cell culture supernatants, mouse serum samples, or recombinant antibody samples were analyzed for neutralizing antibody responses using a vesicular stomatitis virus (VSV)–based pseudovirus neutralization assay. Codon-optimized SARS-CoV-2 full-length spike genes were cloned into a pCAGGS expression vector. The recombinant VSVΔG-based SARS-CoV-2 pseudovirus was generated by transfecting BHK-21/WI-2 cells with the spike expression plasmid, followed by infection with VSVΔG-firefly-luciferase, as described previously (*45*). For neutralization assays, A549 cells expressing hACE2 and transmembrane serine protease 2 (TMPRSS2) were used as target cells. For mouse serum, samples were heat inactivated for 45 min at 56°C and serially diluted in Dulbecco's modified Eagle's medium (DMEM) supplemented with 10% fetal bovine serum (FBS). The diluted samples or culture medium (serving as virus-only control) were mixed with VSVΔG-based SARS-CoV-2 pseudovirus and incubated at 37°C for 45 min. The inoculum-virus or virus-serum mix was subsequently used to infect A549-hACE2-TMPRSS2 cells for 18 hours at 37°C. After the incubation, an equal volume of One-Glo reagent (Promega, E6120) was added to the culture medium for readout. Luminescence was measured and percent neutralization was calculated on the basis of relative luminescence units of the virus-only control for single concentration screening, or IC_{50} was determined using a four-parameter logistic regression model for serial dilution titrations (GraphPad Prism v.9).

VHH sequencing and VHH humanization

Frozen, single-cell sorted VHH^+ llama B cells were selected for sequencing on the basis of supernatant screening. Briefly, single cells were thawed on ice, and mRNA was extracted using the Dynabeads mRNA Purification Kit (Invitrogen, A33562) and eluted into tris-HCl. Complementary deoxyribonucleic acid (cDNA) preparation was performed using ProtoScript II First Strand cDNA Synthesis Kit (NEB, E6560L). VHH HC sequences were amplified by nested polymerase chain reaction (PCR) using Q5 High-fidelity DNA polymerase (NEB, M0491S), using 10 μM llama IgG-specific primers (CAL001 and CAL002). Sense primers used in the second round of nested PCR (VHH specific) were modified to include i5 and i7 adapter sequences to facilitate subsequent MiSeq sequencing (57-Ad primer, NGS-Lam07, NGS-Lam08).

Primers/probe sequences for VHH amplification included Cal001 forward primer: 5′-GTC CTG GCT GCT CTT CTA CAA GG-3′; Cal002 reverse primer: 5′-GGT ACG TGC TGT TGA ACT GTT CC-3′; 57-Ad forward primer: 5′-TCG TCG GCA GCG TCA GAT GTG TAT AAG AGA CAG GCT CTT CTA CAA GG-3′; NGS-Lam07 reverse primer: 5′-GTC TCG TGG GCT CGG AGA TGT GTA TAA GAG ACA GTG GTT GTG GTT TTG GTG TCT TGG GTT-3′; and NGS-Lam08 reverse primer: 5′-GTC TCG TGG GCT CGG AGA TGT GTA TAA GAG ACA GGG AGC TGG GGT CTT CGC TGT GGT GCG-3′.

Index barcode primers (designed from Illumina) were then added in a third index PCR using Hot Start KAPA Ready Mix (Roche, KK2602). Reactions were pooled and purified using AmPure solid-phase reversible immobilization beads (Beckman Coulter, A63881), and the library was sequenced using a MiSeq Reagent Kit v3 600-cycle (Illumina, MS-102-3003). Raw sequencing data were analyzed via MiXCR (v4.6.0), using a custom reference library of llama and alpaca VHH sequences. Clonal expansions were identified by sequence alignments of variable regions with matching V and J gene usage, identical complementarity-determining region 3 (CDR3) length, and ≥80% amino acid identity in the CDR3 region. Selected VHH amino acid sequences were produced recombinantly via transient transfection of CHO-K1 cells (Biointron Biologicals, Inc).

VHH HC sequences were humanized by framework-region engineering. VHH amino acid sequences were aligned to the closest human germline sequences identified using the international ImMunoGeneTics information system (IMGT) database, which was also used to annotate framework regions (FWRs) and complementarity-determining regions (CDRs). Humanizing substitutions were restricted to FWRs; no changes were introduced into CDRs. For each VHH, amino acid differences between the parental VHH sequence and the corresponding human germline reference sequence were identified across the FWRs. Each nonidentical VHH residue was evaluated against the IMGT human germline database to determine its frequency among human germline sequences. VHH residues present in less than 40% of human germline sequences at the corresponding position were mutated to the humanized residue. All FWR positions were considered except cysteine residues required for proper folding and residues in the conserved VHH tetrad motif.

Competition assay

Antibodies were epitope binned using a sandwich competition assay on the Carterra LSA platform, as previously described (*46*). Briefly, experiments were performed at room temperature using a preactivated HCX-30M chip (Carterra, 4279). The sample and fluidics compartment (SFC and 96PH) were primed in running buffer containing 25 mM 2-(*N*-morpholino)ethanesulfonic acid (pH 5.5) (Carterra, 3625) and 0.01% Tween 20. Test antibodies, including five reference antibodies (GC2225, BD55-1205, VYD222, SA55, and S309) (*19*, *47*), were diluted to 5 μg/ml and immobilized onto the chip. A classic binning script was used, involving a coinjection format of sample delivery, in which antigen (200 nM) and the competing antibody (200 nM) were injected with minimal dissociation time. Typical association times ranged from 3 to 5 min. Surfaces were regenerated with 75 mM phosphoric acid after each binning cycle. All data were analyzed using Carterra's Epitope software.

The hACE2 competition assay was run on the Sartorius Octet biolayer interferometry platform, as previously described (*20*). Briefly, 100 nM recombinant HC-only antibody (HCAb) or reference IgG was loaded onto AHC sensors (Sartorius, 18-5064) for 10 min, then quenched using 300 nM an anti-influenza HCAb to block

Downloaded from https://www.science.org at Cambridge University on October 18, 2026

unoccupied binding sites. Antibody-loaded sensors were next associated with 100 nM SARS-CoV-2 XBB.1.5 RBD (AcroBiosystems, SPD-C5242) and competed with 100 nM hACE2-Fc (Sino Biological, 10108-H02H). Data were analyzed using Octet Analysis Studio software.

Protein production and complex formation for x-ray structure determination

Purified MOD225, MOD203, and MOD239 VHHs were produced by transient transfection (Biointron Biologicals Inc.). Briefly, codon-optimized cDNAs encoding each VHH, including a C-terminal His-tag, were synthesized, subcloned into the pcDNA3.4 vector, and sequence verified. The VHH proteins were expressed in CHO-K1 cells via transient electroporation. Four days after transfection, conditioned medium was harvested and applied to Ni magnetic beads for affinity purification. Eluates were subsequently dialyzed into PBS.

The SARS-CoV-2 KP.3 RBD (residues 330 to 528) was synthesized with a C-terminal human rhinovirus 3C (HRV3C) protease cleavage site followed by both a His-tag and a Strep-tag II. The construct was subcloned into pcDNA3.4, sequence verified (GeneImmune), and transiently expressed in Expi293F GnTI$^-$ cells (Thermo Fisher Scientific, A39240) using Turbo293 transfection reagent (Speed Biosystems, PXX1006). Five days after transfection, supernatants were harvested and purified using Strep-Tactin XT 4Flow resin (IBA, 2-1250-025), then buffer-exchanged into HRV3C cleavage buffer and treated with HRV3C protease (Thermo Fisher Scientific, 88946). The reaction mixture was passed over nickel–nitrilotriacetic acid resin (Thermo Fisher Scientific, 88222) to remove the protease, cleaved tags, and any uncleaved RBD. Final purification was performed by SEC on a Superdex 200 Increase 10/300 GL column (Cytiva, 17517501) in PBS.

For complex formation, each VHH (MOD225, MOD203, and MOD239) was individually mixed with KP.3 RBD at a 1:1.2 molar ratio (RBD:VHH). Complexes were concentrated using a 10-kDa molecular weight cutoff (MWCO) centrifugal concentrator (Millipore, UFC5010) and purified by SEC on a Superdex 200 Increase 10/300 GL column equilibrated in 10 mM Hepes, pH 7.4, and 150 mM NaCl to isolate the complexes and perform buffer exchange. The final protein concentrations used for crystallization screening were 16 mg/ml for MOD225–KP.3 RBD and 12 mg/ml for both MOD203–KP.3 RBD and MOD239–KP.3 RBD complexes.

Protein crystallization and structure determination

Crystallization screening of KP.3 RBD complexes with MOD225, MOD203, and MOD239 VHHs was performed at 20°C using an SPT Labtech Mosquito robot and commercial screens. Drops were set at a 1:1 ratio (50 nl of protein complex:50 nl of reservoir). An initial crystallization hit for the KP.3 RBD–MOD225 complex was identified in 0.2 M sodium iodide and 20% (w/v) polyethylene glycol (PEG) 3350 (Red Wings screen, Hampton Research, HR2-073). This condition was optimized to 0.2 M sodium iodide and 17.5% (w/v) PEG 3350 in hanging-drop format with a drop ratio of 0.4 μl of protein complex to 0.5 μl of reservoir. Crystals were cryoprotected using reservoir solution supplemented with 20% (v/v) ethylene glycol. Diffraction data were collected at the National Synchrotron Light Source II (Brookhaven National Laboratory), beamline 19-ID (NYX), using a Dectris Eiger2 9M XE detector. Initial crystallization conditions for the KP.3 RBD–MOD203 and KP.3 RBD–MOD239 complexes were identified using the PEGRx screen (Hampton Research). Crystals of the RBD-MOD203 complex formed in 100 mM sodium citrate tribasic dihydrate (pH 5.0) and 30% (v/v) PEG MME 550; crystals of the RBD-MOD239 complex formed in 100 mM sodium citrate tribasic dihydrate (pH 5.0) and 18% (w/v) PEG 20,000. These conditions were optimized to 32% (v/v) PEG MME 550 for MOD203 and 13% (w/v) PEG 20,000 for MOD239. Optimization was performed in hanging-drop format at a 1:1 drop ratio (0.5 μl of protein complex to 0.5 μl of reservoir). Crystals were cryoprotected in reservoir solution supplemented with 20% (v/v) ethylene glycol for MOD203 and 25% (w/v) glycerol for MOD239. Diffraction data were collected at the Advanced Light Source, beamline 4.2.2, using an RDI_8M complementary metal-oxide semiconductor (CMOS) detector. Diffraction data for all complexes were processed using XDS (*48*), POINTLESS (*49*), and AIMLESS (*50*). Resolution cutoffs were 2.35 Å for RBD-MOD225, 1.90 Å for RBD-MOD203, and 2.10 Å for RBD-MOD239. The RBD-MOD225 complex crystallized in space group $P3_121$ with unit cell dimensions $a = b = 86.0$, $c = 121.0$ Å ($\alpha = \beta = 90°$, $\gamma = 120°$). The RBD-MOD203 complex crystallized in $P3_221$ with $a = b = 136.5$, $c = 45.3$ Å ($\alpha = \beta = 90°$, $\gamma = 120°$). The RBD-MOD239 complex crystallized in $P1$ with unit cell dimensions $a = 47.8$, $b = 69.7$, $c = 75.4$ Å ($\alpha = 83.6°$, $\beta = 82.7°$, $\gamma = 89.9°$). The asymmetric unit contained one complex each for RBD-MOD225 and RBD-MOD203 and two complexes for RBD-MOD239. Structures were solved by molecular replacement using PHASER (*51*) in Collaborative Computational Project Number 4 (CCP4) suite (*52*), with PDB ID 8QH1 as the search model for the RBD. Nanobody search models included PDB ID 9G48 for MOD225 and 7KN7 for MOD203 and MOD239. Refinement was performed using REFMAC5 (CCP4 suite) (*53*), and model building was carried out in COOT (*54*). Data collection and refinement statistics are provided in table S1. Final coordinates and structure factors have been deposited in the PDB under accession codes 9YZ7 (MOD225), 9YZ8 (MOD203), and 9YZ9 (MOD239).

Viral antibody escape assay

A replication-competent recombinant VSV (rVSV)–based system pseudotyped with the XBB.1.16.9 spike protein was used to evaluate viral escape from mAb pressure, as previously reported (*19*). Briefly, 24-well plates seeded with a monolayer of Vero E6 cells were infected with rVSV–SARS-CoV-2 pseudovirus at a multiplicity of infection (MOI) of 0.01 and incubated at 37°C for 1 hour. After incubation, the inoculum was removed and mAbs were added at a concentration corresponding to the 90% inhibitory concentration (IC_{90}). The infected cells were maintained at 37°C for 3 to 4 days until extensive cytopathic effect (CPE) was observed, after which the viral supernatant was harvested. Viral cultures were subjected to 10 sequential passages under continuous antibody pressure. At each passage, viral supernatants were collected for downstream analysis. For mutation profiling, viral RNA was extracted and subjected to Illumina next-generation sequencing (NGS). Mutations were identified by comparing the spike protein sequences of viral populations from each passage with the parental reference sequence, enabling characterization of antibody escape variants. Mutations detected at frequencies above 2% were reported. Antibodies were run in duplicate.

KP.3 RBD DMS for antibody escape mapping

DMS for IgG or HCAb escape mapping was performed as described previously using the SARS-CoV-2 KP.3 RBD (residues N331-T531, SARS-CoV-2 reference numbering) (*7*, *55*). Briefly, each RBD variant

Downloaded from https://www.science.org at Cambridge University on October 18, 2026

was generated via site-directed mutagenesis PCR, fused with an N-terminal hemagglutinin tag and a C-terminal MYC tag, and linked to a unique random 26-nucleotide barcode. The mutant libraries were cloned into the pETcon vector and electroporated into DH10B cells for plasmid amplification (Addgene, 166782). The barcode-variant linkage dictionary was established using PacBio Sequel II single-molecule real-time sequencing. Plasmids were subsequently transformed into *Saccharomyces cerevisiae* strain EBY100 as previously reported. Transformed yeast cells were selected on synthetic dextrose–casamino acid (SD-CAA) plates, expanded in SD-CAA liquid medium, flash-frozen in liquid nitrogen, and stored at −80°C.

High-throughput mutation escape profiling for each mAb or HCAb was conducted using magnetic bead sorting. To ensure library quality, properly folded RBD variants were enriched by removing improperly folded variants using ACE2 (Sino Biological, 10108-H08H-B) conjugated to biotin-binder beads (Thermo Fisher Scientific, 11533D). After a PBS–bovine serum albumin (0.2 mg/ml) wash, the bead-captured, RBD-expressing yeast cells were released, expanded in SD-CAA, and cryopreserved at −80°C. For antibody escape profiling, the ACE2-enriched yeast library was thawed in SD-CAA overnight and subcultured into SG-CAA to induce RBD surface expression. To isolate escape mutants, two sequential rounds of negative selection were performed with a specific antibody to deplete strong binders. This was followed by a positive selection step using anti–c-Myc magnetic beads (Thermo Fisher Scientific, 88843) to capture yeast cells that expressed RBD but escaped antibody binding. The resulting yeast population was washed, grown overnight in SD-CAA, and subjected to plasmid extraction using a 96-well yeast plasmid extraction kit (Coolaber, PE053). The N26 barcode was amplified from the extracted plasmids, purified using 1× AmPure XP beads (Beckman Coulter, A63882), and analyzed via single-end sequencing.

Barcode sequences from both the antibody-screened and reference libraries were mapped to the barcode-variant dictionary. Ambiguous barcodes were excluded, and only barcodes detected more than five times in the reference library were retained for analysis. The escape score for a variant X was calculated as

$$F \times \frac{n_{X,\mathrm{ab}} / N_{\mathrm{ab}}}{n_{X,\mathrm{ref}} / N_{\mathrm{ref}}}$$

In the formula above, F is a scaling factor normalizing scores to a 0 to 1 range, n represents the count of detected barcodes for variant X, and N represents the total barcode count in either the antibody-screened or reference samples.

Generation of mRNA and LNPs

LNP encapsulation of mRNA for antibody delivery was synthesized as previously described. Briefly, sequence-optimized mRNA encoding antibodies were synthesized in vitro using optimized T7 RNA polymerase–mediated transcription reaction with complete replacement of N1-methylpseuduridine. The reactions included a DNA template containing an open reading frame flanked by 5′ untranslated region (UTR) and 3′UTR sequences with a terminal encoded polyA tail. Free mRNA was purified, buffer exchanged, and sterile filtered. LNP-formulated mRNA was produced through a modified ethanol-drop nanoprecipitation process (*22*). Briefly, ionizable, structural, helper, and polyethylene glycol lipids were mixed with mRNA in acetate buffer at a pH of 5.0 and at a ratio of 3:1 (lipids:mRNA). The mixture was neutralized with tris-Cl at a pH of 7.5, sucrose was added as a cryoprotectant, and the final solution was sterile filtered. Formulated LNPs were stored frozen at −80°C and thawed once before dosing. All formulations underwent analytical characterization for particle size, RNA encapsulation, mRNA purity, osmolarity, and endotoxin.

Mouse studies to evaluate serum antibody expression and half-life

Homozygous Tg32-SCID mice [B6.Cg-Fcgrt^{tm1Dcr} Prkdcscid Tg(FCGRT)32Dcr/DcrJ] (the Jackson Laboratory, 018441) or C57BL/6 mice (Charles River Laboratories) were used for serum half-life and Fc homodimerization expression studies, respectively. Animals were housed in groups of four or five, fed standard chow diets, subjected to a photoperiod of a 12-hour light/dark cycle, and kept at an ambient animal room temperature of 70° ± 2°F (21.11° ± 1.11°C) with a room humidity of 50 ± 5%.

For serum half-life studies, 6- to 8-week-old female Tg32-SCID mice (four to eight mice per group) were injected via the tail vein with the indicated mRNA-LNP at a dose of 0.5 mg/kg in 100 μl total volume. For Fc-homodimerization studies, 8-week-old female C57BL/6 mice (5 mice per group) were injected via the tail vein with the indicated mRNA-LNP at a dose of 1 mg/kg in 100 μl total volume. Mice were bled via the submandibular vein at the indicated time points, and serum was collected for antibody quantification by ELISA and assessment of serum neutralization titer. At the final indicated time point, mice were euthanized via CO_2 asphyxiation and a terminal bleed was collected via cardiac puncture.

Humanized ACE2 mouse protection study

Thirty 6- to 8-week-old, female, hACE2 AC70 mice (Taconic Biosciences, 18222-F, tg/wt) were obtained and randomized into two groups: Control group 1 contained 18 animals, and test group 2 contained 12 animals. On day −1, mRNA-LNPs (0.5 mg/kg) or vehicle control was administered intravenously to mice. On day 0, mice were anesthetized by injecting ketamine (80 mg/kg) and xylazine (5 mg/kg) via the intramuscular route and challenged with SARS-CoV-2 Omicron variant XBB.1.5 (BEI Resources, NR-59105). The challenge virus was administered intranasally, dropwise, using a total volume of 50 μl per animal (25 μl per nostril). The stock titer was determined by plaque assay as 3.93×10^5 PFU/ml and used undiluted to give ~1.96×10^4 PFU per mouse in 50 μl total volume, as predetermined in titration studies performed by BIOQUAL Inc. Scheduled necropsy occurred on day 4 for half the animals in each group ($n = 9$ in group 1, $n = 6$ in group 2). Whole lungs were collected and sectioned into separate pieces for PCR or 50% tissue culture infectious dose ($TCID_{50}$) analysis. Each section was weighed, recorded, and individually snap-frozen at −80°C until analysis. The remaining animals were monitored daily for body weight, clinical observation, and survival until day 14.

$TCID_{50}$ assay to determine SARS-CoV-2 infectious titers

Lung tissue sections were homogenized in 0.5 ml of cold medium [DMEM +10% FBS + puromycin + penicillin-streptomycin (P/S)] for ~20 s using a handheld tissue homogenizer (Omni International, Kennesaw, GA). The samples were centrifuged at 2000*g* at 4°C for 10 min. The supernatant was then pipetted through a 100-μm strainer into the original vial for use in viral load determination. The $TCID_{50}$ assay was conducted according to BIOQUAL standard procedures.

Downloaded from https://www.science.org at Cambridge University on October 18, 2026

Briefly, clear, flat-bottom, 96-well culture microplates (BD Falcon, 353072) were seeded with Vero TMPRSS2 cells (25,000 cells per well in DMEM +10% FBS + Puro + P/S) and incubated at 37°C, 5.0% CO_2 until 80 to 100% confluence. The growth medium was aspirated and replaced with 180 μl per well of infection medium (DMEM +2% FBS + Puro + P/S); 20 μl of processed tissue sample or positive/negative control was added to the top row of the plate in quadruplicate, mixed via pipetting, and then serially diluted 10-fold down the plate using fresh pipette tips between rows. The plates were incubated at 37°C, 5.0% CO_2 for 4 days. After incubation, the cell monolayers were visually inspected for CPE. The $TCID_{50}$ per milliliter was calculated using the Reed-Muench formula and adjusted on the basis of the tissue section weight, homogenization volume, and sample volume used in the assay to calculate $TCID_{50}$ titer per gram of tissue.

RT-qPCR assay

Reverse transcription quantitative polymerase chain reaction (RT-qPCR)–based measurements of viral load in lung tissue were performed by BIOQUAL. The RT-qPCR assay for SARS-CoV-2 genomic RNA (gRNA) used primers and a probe specifically designed to amplify and bind to a conserved region of the nucleocapsid (N) gene of SARS-CoV-2, and the assay for subgenomic RNA (sgRNA) used primers and a probe specifically designed to amplify and bind to a region of the envelope (E) gene mRNA from SARS-CoV-2, which is not packaged into the virion.

Primers/probe sequences for gRNA amplification included 2019-nCoV forward primer: 5′-GAC CCC AAA ATC AGC GAA AT-3′; 2019-nCoV reverse primer: 5′-TCT GGT TAC TGC CAG TTG AAT CTG-3′; and 2019-nCoV P: 5′-FAM-ACC CCG CAT /ZEN/ TAC GTT TGG TGG ACC-BHQ1-3′. Primers/probe sequences for sgRNA amplification included Sg-E forward primer: 5′-CGA TCT CTT GTA GAT CTG TTC TC-3′; E Sarbeco R2 reverse primer: 5′-ATA TTG CAG CAG TAC GCA CAC A-3′; and E Sarbeco P1: 5′-/FAM-ACA CTA GCC ATC CTT ACT GCG CTT CG-BBQ-3′.

Viral RNA was extracted from lungs by homogenizing tissue samples in 1 ml of RNA STAT-60 (Tel-Test, Inc.) and processed according to manufacturer instructions to precipitate, purify, and resuspend in RNase-free water. To generate standard curves, a SARS-CoV-2 N gene (gRNA) or E gene (sgRNA) sequence was synthesized and cloned into a puc57 plasmid (GenScript), quantified, and serially diluted into RNase-free water to create a standard curve from 1 to 10^7 copies per 5-μl sample. SensiFAST Probe Lo-ROX One-Step Kit (Meridian Bioscience, BIO-78001) was used to prepare a master mix according to manufacturer's instructions. The final reaction mix contained 600 nM primers (forward and reverse each) and 140 nM probes. In a 96-well reaction plate (Applied Biosystems, N801-0560), 45 μl of the master mix was added to each well followed by 5 μl of sample (in triplicate), positive control, or no template control. Plates were sealed with optical film and amplified on the Applied Biosystems 7500 Real-Time PCR System using the following program: 48°C for 30 min, 95°C for 10 min, followed by 40 cycles of 95°C for 15 s and 55°C for 1 min. The number of RNA copies per gram of tissue was calculated using the standard curve and adjusted by the tissue sample weight (in grams), extraction volume, and sample dilution factor (if applicable).

Sample preparation for MS analysis

Cell culture medium was first clarified through centrifugation at 4000*g* for 20 min followed by filtration using a 0.22-μm filter (Millipore, GPWP04700). Filtered medium was then incubated with Protein A/G magnetic beads (Thermo Fisher Scientific, 88803) under constant rotation for 1 hour at room temperature. After incubation, beads were washed three times with PBS and three times with MS-grade water. Enriched antibodies were eluted using 0.1% formic acid in MS-grade water and stored at −80°C until MS analysis.

Serum samples were first diluted with PBS (pH 7.4) in a 1:1 v/v ratio before incubation with streptavidin-functionalized magnetic beads (Cytiva, 30152105010150) conjugated to biotin-labeled goat anti-Human Fc IgG (Thermo Fisher Scientific, 13-4998-83). Samples were incubated under constant rotation for 1 hour at room temperature followed by three washes with PBS and three washes with MS-grade water. Enriched antibodies were eluted using 0.1% formic acid in MS-grade water and dried down using a nitrogen evaporator. Pellets were resuspended in 100 mM triethylammonium bicarbonate (TEAB) in MS-grade water, and 10 units of peptide:*N*-glycosidase F (PNGase-F; NEB, P0704L) was added to each sample. Overnight incubation was performed at 37°C followed by acidification with formic acid to a final concentration of 0.1%. Samples were stored at −80°C until MS analysis.

Intact MS data acquisition and analysis of Fc homodimerization efficiency

Samples were thawed and loaded into autosampler vials for analysis on an Exploris 480 hybrid mass spectrometer coupled to a Vanquish Neo ultrahigh-performance liquid chromatography (Thermo Fisher Scientific). Samples were separated using a 150 μm–by–15 cm MabPac reverse phase column (Thermo Fisher Scientific, 164947) using an aqueous phase of 0.1% formic acid in LC-MS water (A) and an organic phase of 80% acetonitrile, 19.9% LC-MS water, and 0.1% formic acid (B). The following gradient was used: 10% B to 95% B from 0 to 20 min, 95% B held for 5 min followed by column wash and equilibration. MS data were acquired at the MS1 level with the following source settings: positive voltage of 2100 V, ion transfer tube temperature of 320°C, and source fragmentation set to 20 V. Intact MS1 data were collected at 7500 resolution with an automatic gain control target of 300%, an accumulation time of 200 ms, and five microscans per cycle. Pressure in the orbitrap was set to low pressure and a scan range of 1400 to 6000 m/z (mass/charge ratio) was used. Data were analyzed using Biopharma Finder 5.2 (Thermo Fisher Scientific) using the Intact Mass analysis mode. Sliding Window analysis was performed with the ReSpect algorithm. A center target deconvolution mass of 150,000 Da was used. All other settings remained unchanged from the default.

Statistical analysis

Individual-level data are presented in data file S2. Data were analyzed using GraphPad Prism 9 or 10. ELISA titers, serum antibody concentrations, neutralization IC_{50} values, and serum neutralization titers were calculated by four-parameter nonlinear regression. Pharmacokinetic profiles were fitted using a log-scale Bateman model. Survival curves were compared using the log-rank Mantel-Cox test. Longitudinal body-weight data were analyzed using a two-way mixed-effects model with Holm-Šidák multiple-comparisons testing. Infectious lung viral titers and viral RNA abundance were compared using two-tailed unpaired Student's t tests without log transformation. Matched serum neutralization measurements were analyzed using the Friedman test. Data are presented as indicated in the figure legends, including geometric mean ± SD or median with

Downloaded from https://www.science.org at Cambridge University on October 18, 2026

95% confidence interval (CI). No outliers were excluded. For analyses using parametric statistical tests, normality was assessed by visual inspection of Q-Q plots and the Shapiro-Wilk test, and no substantial deviations from normality were observed. Technical replicates and numbers of independent experiments are specified in the figure legends. *n* represents the number of biological replicates, and *N* represents the number of independent experiments. Statistical significance was defined as ns (not significant); $*P < 0.05$; $**P < 0.01$; $***P < 0.001$; and $****P < 0.0001$.

Supplementary Materials

The PDF file includes:
Figs. S1 to S6
Tables S1 and S2

Other Supplementary Material for this manuscript includes the following:
Data files S1 and S2
MDAR Reproducibility Checklist

REFERENCES AND NOTES

1. R. A. Evans, S. Dube, Y. Lu, M. Yates, S. Arnetorp, E. Barnes, S. Bell, L. Carty, K. Evans, S. Graham, N. Justo, P. Moss, S. Venkatesan, R. Yokota, C. Ferreira, R. McNulty, S. Taylor, J. K. Quint, Impact of COVID-19 on immunocompromised populations during the Omicron era: Insights from the observational population-based INFORM study. *Lancet Reg. Health Eur.* **35**, 100747 (2023).
2. M. J. Levin, A. Ustianowski, S. De Wit, O. Launay, M. Avila, A. Templeton, Y. Yuan, S. Seegobin, A. Ellery, D. J. Levinson, P. Ambery, R. H. Arends, R. Beavon, K. Dey, P. Garbes, E. J. Kelly, G. C. K. W. Koh, K. A. Near, K. W. Padilla, K. Psachoulia, A. Sharbaugh, K. Streicher, M. N. Pangalos, M. T. Esser, PROVENT Study Group, Intramuscular AZD7442 (tixagevimab-cilgavimab) for prevention of COVID-19. *N. Engl. J. Med.* **386**, 2188–2200 (2022).
3. A. Gupta, Y. Gonzalez-Rojas, E. Juarez, M. Crespo Casal, J. Moya, D. R. Falci, E. Sarkis, J. Solis, H. Zheng, N. Scott, A. L. Cathcart, C. M. Hebner, J. Sager, E. Mogalian, C. Tipple, A. Peppercorn, E. Alexander, P. S. Pang, A. Free, C. Brinson, M. Aldinger, A. E. Shapiro, COMET-ICE Investigators, Early treatment for COVID-19 with SARS-CoV-2 neutralizing antibody sotrovimab. *N. Engl. J. Med.* **385**, 1941–1950 (2021).
4. D. M. Weinreich, S. Sivapalasingam, T. Norton, S. Ali, H. Gao, R. Bhore, B. J. Musser, Y. Soo, D. Rofail, J. Im, C. Perry, C. Pan, R. Hosain, A. Mahmood, J. D. Davis, K. C. Turner, A. T. Hooper, J. D. Hamilton, A. Baum, C. A. Kyratsous, Y. Kim, A. Cook, W. Kampman, A. Kohli, Y. Sachdeva, X. Graber, B. Kowal, T. DiCioccio, N. Stahl, L. Lipsich, N. Braunstein, G. Herman, G. D. Yancopoulos, Trial Investigators, REGN-COV2, a neutralizing antibody cocktail, in outpatients with COVID-19. *N. Engl. J. Med.* **384**, 238–251 (2021).
5. P. Chen, A. Nirula, B. Heller, R. L. Gottlieb, J. Boscia, J. Morris, G. Huhn, J. Cardona, B. Mocherla, V. Stosor, I. Shawa, A. C. Adams, J. Van Naarden, K. L. Custer, L. Shen, M. Durante, G. Oakley, A. E. Schade, J. Sabo, D. R. Patel, P. Klekotka, D. M. Skovronsky, SARS-CoV-2 neutralizing antibody LY-CoV555 in outpatients with COVID-19. *N. Engl. J. Med.* **384**, 229–237 (2021).
6. D. Focosi, "Monoclonal antibody therapies against SARS-CoV-2: Promises and realities" in *Convalescent Plasma and Other Antibody Therapies for Infectious Diseases*, N. Paneth, M. J. Joyner, A. Casadevall, Eds. (Springer, 2024), pp. 131–147.
7. Y. Cao, J. Wang, F. Jian, T. Xiao, W. Song, A. Yisimayi, W. Huang, Q. Li, P. Wang, R. An, J. Wang, Y. Wang, X. Niu, S. Yang, H. Liang, H. Sun, T. Li, Y. Yu, Q. Cui, S. Liu, X. Yang, S. Du, Z. Zhang, X. Hao, F. Shao, R. Jin, X. Wang, J. Xiao, Y. Wang, X. S. Xie, Omicron escapes the majority of existing SARS-CoV-2 neutralizing antibodies. *Nature* **602**, 657–663 (2022).
8. P. Schmidt, Y. Li, M. Popejoy, Immunobridging for pemivibart, a monoclonal antibody for prevention of COVID-19. *N. Engl. J. Med.* **391**, 1860–1862 (2024).
9. G. Haidar, S. Thomas, P. Loubet, R. I. Baker, T. Benfield, J. Boonyaratanakornkit, S. Kiertiburanakul, A. H. J. Kim, E. E. Longbrake, J.-M. Molina, R. Paredes, D. Tucker, A. Uriel, J. Weinmann-Menke, A. A. Aksyuk, L. E. Clegg, A. Currie, H. Yang, K. Flyrin, M. Gibbs, M. Shroff, J. L. Perez, L.-J. Chang, T. S. Cohen, SUPERNOVA study group, Efficacy and safety of sipavibart for prevention of COVID-19 in individuals who are immunocompromised (SUPERNOVA): A randomised, controlled, double-blind, phase 3 trial. *Lancet Infect. Dis.* **25**, 813–826 (2025).
10. Q. Wang, Y. Guo, I. A. Mellis, M. Wu, H. Mohri, C. Gherasim, R. Valdez, L. J. Purpura, M. T. Yin, A. Gordon, D. D. Ho, Antibody evasiveness of SARS-CoV-2 subvariants KP.3.1.1 and XEC. *Cell Rep.* **44**, 115543 (2025).
11. Y. Cai, S. Diallo, K. Rosenthal, K. Ren, D. J. Flores, A. Dippel, V. Oganesyan, N. van Dyk, X. Chen, E. Cantu, R. Choudhary, M. Sulikowski, H. Adissu, B. Chawla, S. Kar, C. Liu, A. Dijokaite-Guraliuc, J. Mongkolsapaya, S. Rajan, Y. M. Loo, R. Beavon, C. Webber, L. J. Chang, S. Thomas, L. Clegg, H. Zhang, G. R. Screaton, N. Philbin, M. Harre, A. Selim, N. Martinez-Alier, A. Uriel, T. S. Cohen, J. L. Perez, M. T. Esser, W. Blair, J. R. Francica, AZD3152 neutralizes SARS-CoV-2 historical and contemporary variants and is protective in hamsters and well tolerated in adults. *Sci. Transl. Med.* **16**, eado2817 (2024).
12. E. K. Wagner, J. A. Maynard, Engineering therapeutic antibodies to combat infectious diseases. *Curr. Opin. Chem. Eng.* **19**, 131–141 (2018).
13. M. S. Karbyshev, I. V. Kalashnikova, V. V. Dubrovskaya, K. O. Baskakova, P. K. Kuzmichev, V. Sandig, Trends and challenges in bispecific antibody production. *J. Chromatogr. A* **1744**, 465722 (2025).
14. Z. Li, S. Li, G. Zhang, W. Peng, Z. Chang, X. Zhang, Z. Fan, Y. Chai, F. Wang, X. Zhao, D. Li, R. Zhang, Z. He, W. Zou, K. Xu, W. Lei, P. Liu, J. Hao, J. Zhang, L. Sun, G. Wu, S. Tan, G. F. Gao, F. Gao, Y. Wu, An engineered bispecific human monoclonal antibody against SARS-CoV-2. *Nat. Immunol.* **23**, 423–430 (2022).
15. H. Cho, K. K. Gonzales-Wartz, D. Huang, M. Yuan, M. Peterson, J. Liang, N. Beutler, J. L. Torres, Y. Cong, E. Postnikova, S. Bangaru, C. A. Talana, W. Shi, E. S. Yang, Y. Zhang, K. Leung, L. Wang, L. Peng, J. Skinner, S. Li, N. C. Wu, H. Liu, C. Dacon, T. Moyer, M. Cohen, M. Zhao, F. E.-H. Lee, R. S. Weinberg, I. Douagi, R. Gross, C. Schmaljohn, A. Pegu, J. R. Mascola, M. Holbrook, D. Nemazee, T. F. Rogers, A. B. Ward, I. A. Wilson, P. D. Crompton, J. Tan, Bispecific antibodies targeting distinct regions of the spike protein potently neutralize SARS-CoV-2 variants of concern. *Sci. Transl. Med.* **13**, eabj5413 (2021).
16. J. Misasi, R. R. Wei, L. Wang, A. Pegu, C. J. Wei, O. K. Oloniniyi, T. Zhou, J. I. Moliva, B. Zhao, M. Choe, E. S. Yang, Y. Zhang, M. Boruszczak, M. Chen, K. Leung, J. Li, Z. Y. Yang, H. Andersen, K. Carlton, S. Godbole, D. R. Harris, A. R. Henry, V. B. Ivleva, Q. P. Lei, C. Liu, L. Longobardi, J. S. Merriam, D. Nase, A. S. Olia, L. Pessaint, M. Porto, W. Shi, S. M. Wallace, J. J. Wolff, D. C. Douek, M. S. Suthar, J. G. Gall, R. A. Koup, P. D. Kwong, J. R. Mascola, G. J. Nabel, N. J. Sullivan, A multispecific antibody against SARS-CoV-2 prevents immune escape in vitro and confers prophylactic protection in vivo. *Sci. Transl. Med.* **16**, eado9026 (2024).
17. Y. Cao, F. Jian, J. Wang, Y. Yu, W. Song, A. Yisimayi, J. Wang, R. An, X. Chen, N. Zhang, Y. Wang, P. Wang, L. Zhao, H. Sun, L. Yu, S. Yang, X. Niu, T. Xiao, Q. Gu, F. Shao, X. Hao, Y. Xu, R. Jin, Z. Shen, Y. Wang, X. S. Xie, Imprinted SARS-CoV-2 humoral immunity induces convergent Omicron RBD evolution. *Nature* **614**, 521–529 (2023).
18. F. Jian, Y. Cao, Deciphering SARS-CoV-2 evolution under antibody immune pressure. *Trends Immunol.* **46**, 263–265 (2025).
19. F. Jian, A. Z. Wec, L. Feng, Y. Yu, L. Wang, P. Wang, L. Yu, J. Wang, J. Hou, D. M. Berrueta, D. Lee, T. Speidel, L. Ma, T. Kim, A. Yisimayi, W. Song, J. Wang, L. Liu, S. Yang, X. Niu, T. Xiao, R. An, Y. Wang, F. Shao, Y. Wang, S. Pecetta, X. Wang, L. M. Walker, Y. Cao, Viral evolution prediction identifies broadly neutralizing antibodies to existing and prospective SARS-CoV-2 variants. *Nat. Microbiol.* **10**, 2003–2017 (2025).
20. C. G. Rappazzo, L. V. Tse, C. I. Kaku, D. Wrapp, M. Sakharkar, D. Huang, L. M. Deveau, T. J. Yockachonis, A. S. Herbert, M. B. Battles, C. M. O'Brien, M. E. Brown, J. C. Geoghegan, J. Belk, L. Peng, L. Yang, Y. Hou, T. D. Scobey, D. R. Burton, D. Nemazee, J. M. Dye, J. E. Voss, B. M. Gunn, J. S. McLellan, R. S. Baric, L. E. Gralinski, L. M. Walker, Broad and potent activity against SARS-like viruses by an engineered human monoclonal antibody. *Science* **371**, 823–829 (2021).
21. M. Yuan, X. Zhu, W. T. He, P. Zhou, C. I. Kaku, T. Capozzola, C. Y. Zhu, X. Yu, H. Liu, W. Yu, Y. Hua, H. Tien, L. Peng, G. Song, C. A. Cottrell, W. R. Schief, D. Nemazee, L. M. Walker, R. Andrabi, D. R. Burton, I. A. Wilson, A broad and potent neutralization epitope in SARS-related coronaviruses. *Proc. Natl. Acad. Sci. U.S.A.* **119**, e2205784119 (2022).
22. A. August, H. Z. Attarwala, S. Himansu, S. Kalidindi, S. Lu, R. Pajon, S. Han, J. M. Lecerf, J. E. Tomassini, M. Hard, L. M. Ptaszek, J. E. Crowe, T. Zaks, A phase 1 trial of lipid-encapsulated mRNA encoding a monoclonal antibody with neutralizing activity against Chikungunya virus. *Nat. Med.* **27**, 2224–2233 (2021).
23. P. Schmidt, K. Narayan, Y. Li, C. I. Kaku, M. E. Brown, E. Champney, J. C. Geoghegan, M. Vasquez, E. M. Krauland, T. Yockachonis, S. Bai, B. M. Gunn, A. Cammarata, C. M. Rubino, P. Ambrose, L. M. Walker, Antibody-mediated protection against symptomatic COVID-19 can be achieved at low serum neutralizing titers. *Sci. Transl. Med.* **15**, eadg2783 (2023).
24. J. Zalevsky, A. K. Chamberlain, H. M. Horton, S. Karki, I. W. Leung, T. J. Sproule, G. A. Lazar, D. C. Roopenian, J. R. Desjarlais, Enhanced antibody half-life improves in vivo activity. *Nat. Biotechnol.* **28**, 157–159 (2010).
25. E. Narayanan, S. Falcone, S. M. Elbashir, H. Attarwala, K. Hassett, M. S. Seaman, A. Carfi, S. Himansu, Rational design and in vivo characterization of mRNA-encoded broadly neutralizing antibody combinations against HIV-1. *Antibodies* **11**, 67 (2022).
26. J. H. Ha, J. E. Kim, Y. S. Kim, Immunoglobulin Fc heterodimer platform technology: From design to applications in therapeutic antibodies and proteins. *Front. Immunol.* **7**, 394 (2016).
27. J. B. Ridgway, L. G. Presta, P. Carter, "Knobs-into-holes" engineering of antibody CH3 domains for heavy chain heterodimerization. *Protein Eng.* **9**, 617–621 (1996).

Downloaded from https://www.science.org at Cambridge University on October 18, 2026

28. H. M. Callaway, K. M. Hastie, S. L. Schendel, H. Li, X. Yu, J. Shek, T. Buck, S. Hui, D. Bedinger, C. Troup, S. M. Dennison, K. Li, M. D. Alpert, C. C. Bailey, S. Benzeno, J. L. Bonnevier, J. Q. Chen, C. Chen, H. Cho, P. D. Crompton, V. Dussupt, K. C. Entzminger, Y. Ezzyat, J. K. Fleming, N. Geukens, A. E. Gilbert, Y. Guan, X. Han, C. J. Harvey, J. M. Hatler, B. Howie, C. Hu, A. Huang, M. Imbrechts, A. Jin, N. Kamachi, G. Keitany, M. Klinger, J. K. Kolls, S. J. Krebs, T. Li, F. Luo, T. Maruyama, M. A. Meehl, L. Mendez-Rivera, A. Musa, C. J. Okumura, B. E. R. Rubin, A. K. Sato, M. Shen, A. Singh, S. Song, J. Tan, J. M. Trimarchi, D. P. Upadhyay, Y. Wang, L. Yu, T. Z. Yuan, E. Yusko, B. Peters, G. Tomaras, E. O. Saphire, Bivalent intra-spike binding provides durability against emergent Omicron lineages: Results from a global consortium. *Cell Rep.* **42**, 112014 (2023).
29. R. Rosenfeld, T. Noy-Porat, A. Mechaly, E. Makdasi, Y. Levy, R. Alcalay, R. Falach, M. Aftalion, E. Epstein, D. Gur, T. Chitlaru, E. B. Vitner, S. Melamed, B. Politi, A. Zauberman, S. Lazar, A. Beth-Din, Y. Evgy, S. Yitzhaki, S. C. Shapira, T. Israely, O. Mazor, Post-exposure protection of SARS-CoV-2 lethal infected K18-hACE2 transgenic mice by neutralizing human monoclonal antibody. *Nat. Commun.* **12**, 944 (2021).
30. H. Ma, Y. Guo, H. Tang, C. K. Tseng, L. Wang, H. Zong, Z. Wang, Y. He, Y. Chang, S. Wang, H. Huang, Y. Ke, Y. Yuan, M. Wu, Y. Zhang, A. Drelich, K. R. Kempaiah, B. H. Peng, A. Wang, K. Yang, H. Yin, J. Liu, Y. Yue, W. Xu, S. Zhu, T. Ji, X. Zhang, Z. Wang, G. Li, G. Liu, J. Song, L. Mu, Z. Xiang, Z. Song, H. Chen, Y. Bian, B. Zhang, H. Chen, J. Zhang, Y. Liao, L. Zhang, L. Yang, Y. Chen, J. Gilly, X. Xiao, L. Han, H. Jiang, Y. Xie, Q. Zhou, J. Zhu, Broad ultra-potent neutralization of SARS-CoV-2 variants by monoclonal antibodies specific to the tip of RBD. *Cell Discov.* **8**, 16 (2022).
31. A. A. Rubio, V. A. Baharani, B. Dadonaite, M. Parada, M. E. Abernathy, Z. Wang, Y. E. Lee, M. R. Eso, J. Phung, I. Ramos, T. Chen, G. El Nesr, J. D. Bloom, P. D. Bieniasz, M. C. Nussenzweig, C. O. Barnes, Bispecific antibodies targeting the N-terminal and receptor binding domains potently neutralize SARS-CoV-2 variants of concern. *Sci. Transl. Med.* **17**, eadq5720 (2025).
32. E. Stadler, M. T. Burgess, T. E. Schlub, S. R. Khan, K. L. Chai, Z. K. McQuilten, E. M. Wood, M. N. Polizzotto, S. J. Kent, D. Cromer, M. P. Davenport, D. S. Khoury, Monoclonal antibody levels and protection from COVID-19. *Nat. Commun.* **14**, 4545 (2023).
33. E. A. F. Simoes, E. Forleo-Neto, G. P. Geba, M. Kamal, F. Yang, H. Cicirello, M. R. Houghton, R. Rideman, Q. Zhao, S. L. Benvin, A. Hawes, E. D. Fuller, E. Wloga, J. M. N. Pizarro, F. M. Munoz, S. A. Rush, J. S. McLellan, L. Lipsich, N. Stahl, G. D. Yancopoulos, D. M. Weinreich, C. A. Kyratsous, S. Sivapalasingam, Suptavumab for the prevention of medically attended respiratory syncytial virus infection in preterm infants. *Clin. Infect. Dis.* **73**, e4400–e4408 (2021).
34. M. Caskey, T. Schoofs, H. Gruell, A. Settler, T. Karagounis, E. F. Kreider, B. Murrell, N. Pfeifer, L. Nogueira, T. Y. Oliveira, G. H. Learn, Y. Z. Cohen, C. Lehmann, D. Gillor, I. Shimeliovich, C. Unson-O'Brien, D. Weiland, A. Robles, T. Kummerle, C. Wyen, R. Levin, M. Witmer-Pack, K. Eren, C. Ignacio, S. Kiss, A. P. West Jr., H. Mouquet, B. S. Zingman, R. M. Gulick, T. Keler, P. J. Bjorkman, M. S. Seaman, B. H. Hahn, G. Fatkenheuer, S. J. Schlesinger, M. C. Nussenzweig, F. Klein, Antibody 10–1074 suppresses viremia in HIV-1-infected individuals. *Nat. Med.* **23**, 185–191 (2017).
35. M. Caskey, D. R. Kuritzkes, Monoclonal antibodies as long-acting products: What are we learning from human immunodeficiency virus (HIV) and coronavirus disease 2019 (COVID-19)? *Clin. Infect. Dis.* **75**, S530–S540 (2022).
36. Z. Ku, X. Xie, J. Lin, P. Gao, B. Wu, A. El Sahili, H. Su, Y. Liu, X. Ye, E. Y. Tan, X. Li, X. Fan, B. C. Goh, W. Xiong, H. Boyd, A. E. Muruato, H. Deng, H. Xia, J. Zou, B. K. Kalveram, V. D. Menachery, N. Zhang, J. Lescar, P. Y. Shi, Z. An, Engineering SARS-CoV-2 specific cocktail antibodies into a bispecific format improves neutralizing potency and breadth. *Nat. Commun.* **13**, 5552 (2022).
37. L. Corey, P. B. Gilbert, M. Juraska, D. C. Montefiori, L. Morris, S. T. Karuna, S. Edupuganti, N. M. Mgodi, A. C. deCamp, E. Rudnicki, Y. Huang, P. Gonzales, R. Cabello, C. Orrell, J. R. Lama, F. Laher, E. M. Lazarus, J. Sanchez, I. Frank, J. Hinojosa, M. E. Sobieszczyk, K. E. Marshall, P. G. Mukwekwerere, J. Makhema, L. R. Baden, J. I. Mullins, C. Williamson, J. Hural, M. J. McElrath, C. Bentley, S. Takuva, M. M. Gomez Lorenzo, D. N. Burns, N. Espy, A. K. Randhawa, N. Kochar, E. Piwowar-Manning, D. J. Donnell, N. Sista, P. Andrew, J. G. Kublin, G. Gray, J. E. Ledgerwood, J. R. Mascola, M. S. Cohen, HVTN 704/HPTN 085 and HVTN 703/HPTN 081 Study Teams, Two randomized trials of neutralizing antibodies to prevent HIV-1 acquisition. *N. Engl. J. Med.* **384**, 1003–1014 (2021).
38. F. Krammer, The human antibody response to influenza A virus infection and vaccination. *Nat. Rev. Immunol.* **19**, 383–397 (2019).
39. D. C. Ekiert, A. K. Kashyap, J. Steel, A. Rubrum, G. Bhabha, R. Khayat, J. H. Lee, M. A. Dillon, R. E. O'Neil, A. M. Faynboym, M. Horowitz, L. Horowitz, A. B. Ward, P. Palese, R. Webby, R. A. Lerner, R. R. Bhatt, I. A. Wilson, Cross-neutralization of influenza A viruses mediated by a single antibody loop. *Nature* **489**, 526–532 (2012).
40. W. K. Tsai, Y. Li, Z. Yin, P. Tran, Q. Phung, Z. Zhou, K. Peng, D. Qin, S. Tam, C. Spiess, J. Brumm, M. Wong, Z. Ye, P. Wu, S. Cohen, P. J. Carter, Nonclinical immunogenicity risk assessment for knobs-into-holes bispecific IgG(1) antibodies. *mAbs* **16**, 2362789 (2024).
41. A. T. Hooper, S. Somersan-Karakaya, S. E. McCarthy, E. Mylonakis, S. Ali, J. Mei, R. Bhore, A. Mahmood, G. P. Geba, P. Dakin, D. M. Weinreich, G. D. Yancopoulos, G. A. Herman, J. D. Hamilton, COVID-19 Phase 2/3 Hospitalized Trial Team, Casirivimab and imdevimab treatment reduces viral load and improves clinical outcomes in seropositive hospitalized COVID-19 patients with nonneutralizing or borderline neutralizing antibodies. *mBio* **13**, e0169922 (2022).
42. D. Li, M. Xu, A. T. Hooper, D. Rofail, K. A. Mohammadi, Y. Chen, S. Ali, T. Norton, D. M. Weinreich, B. J. Musser, J. D. Hamilton, G. P. Geba, Casirivimab + imdevimab accelerates symptom resolution linked to improved COVID-19 outcomes across susceptible antibody and risk profiles. *Sci. Rep.* **13**, 12784 (2023).
43. F. Raffi, R. L. Gottlieb, Monoclonal antibodies in hospitalised patients with COVID-19: The role of SARS-COV-2 serostatus in an evolving pandemic. *Infect. Dis. Ther.* **12**, 735–747 (2023).
44. E. M. Mucker, C. Thiele-Suess, P. Baumhof, J. W. Hooper, Lipid nanoparticle delivery of unmodified mRNAs encoding multiple monoclonal antibodies targeting poxviruses in rabbits. *Mol. Ther. Nucleic Acids* **28**, 847–858 (2022).
45. D. W. Lee, A. Nasir, S. Elbashir, H. Jani, T. Speidel, A. Gorrie, D. Montes Berrueta, P. Martin, S. Tan, Y. J. Hou, K. Hardcastle, D. Edwards, K. Wu, A. Carfi, Y. Budigi, mRNA-1273 vaccines adapted to JN.1 or KP.2 elicit cross-neutralizing responses against the JN.1 sublineages of SARS-CoV-2 in mice. *Vaccine* **54**, 126961 (2025).
46. A. Z. Wec, D. Haslwanter, Y. N. Abdiche, L. Shehata, N. Pedreno-Lopez, C. L. Moyer, Z. A. Bornholdt, A. Lilov, J. H. Nett, R. K. Jangra, M. Brown, D. I. Watkins, C. Ahlm, M. N. Forsell, F. A. Rey, G. Barba-Spaeth, K. Chandran, L. M. Walker, Longitudinal dynamics of the human B cell response to the yellow fever 17D vaccine. *Proc. Natl. Acad. Sci. U.S.A.* **117**, 6675–6685 (2020).
47. Y. Cao, F. Jian, Z. Zhang, A. Yisimayi, X. Hao, L. Bao, F. Yuan, Y. Yu, S. Du, J. Wang, T. Xiao, W. Song, Y. Zhang, P. Liu, R. An, P. Wang, Y. Wang, S. Yang, X. Niu, Y. Zhang, Q. Gu, F. Shao, Y. Hu, W. Yin, A. Zheng, Y. Wang, C. Qin, R. Jin, J. Xiao, X. S. Xie, Rational identification of potent and broad sarbecovirus-neutralizing antibody cocktails from SARS convalescents. *Cell Rep.* **41**, 111845 (2022).
48. W. Kabsch, XDS. *Acta Crystallogr. D Biol. Crystallogr.* **66**, 125–132 (2010).
49. W. Kabsch, Integration, scaling, space-group assignment and post-refinement. *Acta Crystallogr. D Biol. Crystallogr.* **66**, 133–144 (2010).
50. P. R. Evans, G. N. Murshudov, How good are my data and what is the resolution? *Acta Crystallogr. D Biol. Crystallogr.* **69**, 1204–1214 (2013).
51. A. J. McCoy, R. W. Grosse-Kunstleve, P. D. Adams, M. D. Winn, L. C. Storoni, R. J. Read, Phaser crystallographic software. *J. Appl. Crystallogr.* **40**, 658–674 (2007).
52. J. Agirre, M. Atanasova, H. Bagdonas, C. B. Ballard, A. Basle, J. Beilsten-Edmands, R. J. Borges, D. G. Brown, J. J. Burgos-Marmol, J. M. Berrisford, P. S. Bond, I. Caballero, L. Catapano, G. Chojnowski, A. G. Cook, K. D. Cowtan, T. I. Croll, J. E. Debreczeni, N. E. Devenish, E. J. Dodson, T. R. Drevon, P. Emsley, G. Evans, P. R. Evans, M. Fando, J. Foadi, L. Fuentes-Montero, E. F. Garman, M. Gerstel, R. J. Gildea, K. Hatti, M. L. Hekkelman, P. Heuser, S. W. Hoh, M. A. Hough, H. T. Jenkins, E. Jimenez, R. P. Joosten, R. M. Keegan, N. Keep, E. B. Krissinel, P. Kolenko, O. Kovalevskiy, V. S. Lamzin, D. M. Lawson, A. A. Lebedev, A. G. W. Leslie, B. Lohkamp, F. Long, M. Maly, A. J. McCoy, S. J. McNicholas, A. Medina, C. Millan, J. W. Murray, G. N. Murshudov, R. A. Nicholls, M. E. M. Noble, R. Oeffner, N. S. Pannu, J. M. Parkhurst, N. Pearce, J. Pereira, A. Perrakis, H. R. Powell, R. J. Read, D. J. Rigden, W. Rochira, M. Sammito, F. S. Rodriguez, G. M. Sheldrick, K. L. Shelley, F. Simkovic, A. J. Simpkin, P. Skubak, E. Sobolev, R. A. Steiner, K. Stevenson, I. Tews, J. M. H. Thomas, A. Thorn, J. T. Valls, V. Uski, I. Uson, A. Vagin, S. Velankar, M. Vollmar, H. Walden, D. Waterman, K. S. Wilson, M. D. Winn, G. Winter, M. Wojdyr, K. Yamashita, The CCP4 suite: Integrative software for macromolecular crystallography. *Acta Crystallogr. D Struct. Biol.* **79**, 449–461 (2023).
53. A. A. Vagin, R. A. Steiner, A. A. Lebedev, L. Potterton, S. McNicholas, F. Long, G. N. Murshudov, REFMAC5 dictionary: Organization of prior chemical knowledge and guidelines for its use. *Acta Crystallogr. D Biol. Crystallogr.* **60**, 2184–2195 (2004).
54. P. Emsley, B. Lohkamp, W. G. Scott, K. Cowtan, Features and development of Coot. *Acta Crystallogr. D Biol. Crystallogr.* **66**, 486–501 (2010).
55. F. Jian, J. Wang, A. Yisimayi, W. Song, Y. Xu, X. Chen, X. Niu, S. Yang, Y. Yu, P. Wang, H. Sun, L. Yu, J. Wang, Y. Wang, R. An, W. Wang, M. Ma, T. Xiao, Q. Gu, F. Shao, Y. Wang, Z. Shen, R. Jin, Y. Cao, Evolving antibody response to SARS-CoV-2 antigenic shift from XBB to JN.1. *Nature* **637**, 921–929 (2025).

Acknowledgments: We thank our colleagues P. Jorquera, G. Asthagiri, R. Larocca, L. Ma, T. Kim, J. Mixon, D. Stadlbauer, F. Ghantous, N. Nunna, J. Ventura, C. Clark, L. Li, A. Nasir, S. Tan, and W. Yu for laboratory support and discussions. We also thank K. Hardcastle and the Comparative Medicine team at Moderna for planning and executing in vivo expression studies. This research used resources from beamline 19-ID (NYX) of the National Synchrotron Light Source II, a US Department of Energy (DOE) Office of Science User Facility operated for the DOE Office of Science by Brookhaven National Laboratory under contract no. DE-SC0012704. We thank K. Battaile for collecting x-ray diffraction data at the NYX beamline on our behalf. Beamline 4.2.2 of the Advanced Light Source, a DOE Office of Science User Facility under contract no. DE-AC02-05CH11231, is supported in part by the ALS-ENABLE program funded by the National Institutes of Health, National Institute of General Medical Sciences. We thank J. Nix for collecting x-ray diffraction data at the Molecular Biology Consortium beamline on our behalf.

Downloaded from https://www.science.org at Cambridge University on October 18, 2026

We also acknowledge B. Backstedt and his laboratory team at BIOQUAL Inc. for contributions to the methods and performing the in vivo challenge study. **Funding:** This project was funded by Moderna Inc. **Author contributions:** A.Z.W., L.M.W., S.S., and S.P. conceived the study, supervised research, wrote the original manuscript, and reviewed and edited the final manuscript. W.R.S. conceived and supervised research. A. Cho, X.H., A.S., E.N.K., N.B., D.L., P.B.J.R., Y.C., and F.J. developed the experimental methodology for in vitro and in vivo studies. A. Cho, M.F.B., A.R.L., J.H., A.S., N.B., D.M.-B., T.S., D.L., P.B.J.R., and F.J. performed the experiments and collected the data. A.Z.W., A. Cho, A.S., and X.H. analyzed and visualized the data. A. Carfi acquired funding for the study and supervised research. A.Z.W. and S.P. administered and coordinated the project. **Competing interests:** A.Z.W., A. Cho, S.P., X.H., M.F.B., A.R.L., J.H., A.S., N.B., S.S., E.N.K., D.M.-B., T.S., D.L., P.B.J.R., A. Carfi, W.R.S., and L.M.W. are full-time employees and equity holders in Moderna Inc. A.Z.W., N.B., L.M.W., E.N.K., and S.S. are inventors on a provisional patent application related to Fc homodimerization mutations in this manuscript filed by Moderna Inc. Y.C. is listed as an inventor on provisional patent applications describing the BD55-1205 antibody. The BD55-1205 patents are licensed to Moderna (PCT/CN2023/140169, WO2024131826A1, and WO2024131826A9). Y.C. is a cofounder of Singlomics Biopharmaceuticals. F.J. reports no competing interests. **Data, code, and materials availability:** All data associated with this study are present in the paper or the Supplementary Materials. Antibody sequence information is included in data file S1. Numerical source data underlying the graphs are provided in data file S2. Structural coordinates and structure factors have been deposited in the PDB under the following accession codes: KP.3 RBD + VHH MOD203 (9YZ8), KP.3 RBD + VHH MOD225 (9YZ7), and KP.3 RBD + VHH MOD239 (9YZ9). No new code was generated for this study. mRNA-LNP–encoded antibodies and data are available from the corresponding author (L.M.W.) upon request and are subject to a material and data transfer agreement with Moderna Inc. All other materials used or generated in this study are commercially available or will be supplied upon reasonable request.

Submitted 12 March 2026
Resubmitted 1 July 2026
Accepted 4 September 2026
Published 14 October 2026
10.1126/scitranslmed.aeh1292

Downloaded from https://www.science.org at Cambridge University on October 18, 2026

Science Translational Medicine

Orthogonal Fc engineering enables multiplexed delivery of mRNA-encoded bispecific antibodies that constrain viral escape

Anna Z. Wec, Alice Cho, Simone Pecetta, Xiaozhen Hu, Michael F. Bender, Adrian R. Laciak, Jacob Hou, Fanchong Jian, Elif N. Korkmaz, Arvind Sharma, Nathen Bopp, Steve Sazinsky, Daniela Montes-Berrueta, Tessa Speidel, Diana Lee, Pradeep Babu Jagadeesh Reddy, Yunlong Cao, Andrea Carfi, William R. Schief, and Laura M. Walker

Sci. Transl. Med. **18** (871), eaeh1292. DOI: 10.1126/scitranslmed.aeh1292

View the article online
https://www.science.org/doi/10.1126/scitranslmed.aeh1292
Permissions
https://www.science.org/help/reprints-and-permissions

Downloaded from https://www.science.org at Cambridge University on October 18, 2026

Use of this article is subject to the Terms of service

Science Translational Medicine (ISSN 1946-6242) is published by the American Association for the Advancement of Science. 1200 New York Avenue NW, Washington, DC 20005. The title *Science Translational Medicine* is a registered trademark of AAAS.

Copyright © 2026 The Authors, some rights reserved; exclusive licensee American Association for the Advancement of Science. No claim to original U.S. Government Works